THIN FILM LITHIUM NIOBATE MODULATORS AT 1064 NM

FOR CMOS-COMPATIBLE SYSTEMS

by
Navarun Jagatpal

A thesis submitted to the Faculty of the University of Delaware in partial fulfillment of the requirements for the Master in Electrical and Computer Engineering

Spring 2021

THIN FILM LITHIUM NIOBATE MODULATORS AT 1064 NM

FOR CMOS-COMPATIBLE SYSTEMS

by
Navarun Jagatpal

Approved: _____
Dennis Prather, Ph.D.
Professor in charge of thesis on behalf of the Advisory Committee

Approved: _____
Jamie Phillips, Ph.D.
Chair of the Department of Electrical and Computer Engineering

Approved: _____
Levi T. Thompson, Ph.D.
Dean of the College of Engineering

Approved: _____
Louis F. Rossi, Ph.D.
Vice Provost for Graduate & Professional Education and
Dean of the Graduate College

ACKNOWLEDGMENTS

I would like to thank Dr. Dennis Prather for inviting me into his lab group. As a result of working in this group, I have learned a lot about nanofabrication and microelectronic devices. I have also gotten the chance to use specialized laboratory equipment and systems. This has a unique opportunity to develop a set of skills that would not be possible elsewhere.

I would also like to thank all the engineers who have worked in the lab with me over the past few years and offered advice and support. Dr. Prather oversees the Prather Group, which includes professors and graduate students, and he also oversees the employees of his business, Phase Sensitive Innovations (PSI). The number of ongoing projects across the Prather Group and PSI, as well as their depth, their scope, and their complexity, is astonishing. There have been many times when I spoke to a coworker, starting with an extemporaneous comment or question about my laboratory work, and it led to a fruitful discussion that helped me move forward. I would like to thank Andrew Mercante, Naim Ahmed, Victoria Carey, Sean Nelan, Cooper Hurley, Zhanyu Yang, Jesse Buchan, Chris Cullen, Kyle Linderman, Matthew Konkol, Mathew Zablocki, Josh Johnson, Dr. Janusz Murakowski, Dr. Shouyuan Shi, Dr. Garrett Schneider, and Dr. Peng Yao.

I would also like to thank my parents, Arjun Sau and Jyotsna Sau, who have offered a great deal of love and support as I have worked through graduate school. They were both graduate students once upon a time, at the University of Massachusetts, and they have shared stories about their experiences. They have repeatedly stated that no matter what happens, they will continue to support me in life.

TABLE OF CONTENTS

LIST OF TABLES……....vii
LIST OF FIGURES vii
ABSTRACT..... xiii

Chapter

1 INTRODUCTION 1

1.1 Electro-optic modulators 1
1.2 Analog photonic link systems 2
1.3 Millimeter-wave imaging systems 3

2 ELECTRO-OPTIC MODULATOR FUNDAMENTALS 4

2.1 Low-Frequency Operation 4
2.2 High-Frequency Operation..... 12
2.3 System integration..... 16

3 BACKGROUND AND LITERATURE OVERVIEW..... 18

3.1 Choice of Materials for Electro-optic Modulators 18
3.2 Bulk Lithium Niobate..... 18
3.3 Thin Film Lithium Niobate 19

4 ALTERNATE WAVELENGTH MEASUREMENTS OF TFLN MODULATORS ... 26

5 DESIGN OF WAFER-BONDED PHASE MODULATOR IN TFLN AT 1064 NM... 29

6 LOW-FREQUENCY PHASE MODULATOR IN TFLN AT 1064 NM..... 37

6.1 Simulation 38

6.2 Fabrication 40
6.3 Characterization 42

7 HIGH-FREQUENCY PHASE MODULATOR IN TFLN AT 1064 NM 44

7.1 Simulation 44

7.1.1 Simulations in Lumerical MODE Solutions 44
7.1.2 Simulations in Ansys HFSS Electronics Desktop 45

7.2 Fabrication 48
7.3 Characterization 51

8 DESIGN OF INTENSITY MODULATOR IN TFLN AT 1064 NM 54

9 POTENTIAL FOR SYSTEM INTEGRATION 59

9.1 Analog Photonic Link System at 1064 nm 59
9.2 Single-pixel mmW Antenna system at 1064 nm 60

CONCLUSION 63

REFERENCES 64

Appendix
A PERMISSIONS 68

LIST OF TABLES

Table 8.1: Results of simulations of 1×2 MMI, showing the best results for the tapered input and the non-tapered input…….57

LIST OF FIGURES

Figure 1.1: Commercial-off-the-shelf (COTS) electro-optic modulators. Image source: ThorLabs.com. 2

Figure 2.1: (a) Experimental setup for low-frequency characterization of phase modulator and measurement of $V_{\pi,45^\circ}$. (b) Linearly polarized light, at +45°, at the entrance facet of the modulator. (c) Elliptically polarized light at the exit facet of the modulator. (d) Orientation of the axis of the linear polarizer (LP). 8

Figure 2.2: (a) Electro-optic phase modulator. (b) Mach-Zehnder intensity modulator. (c) Microring modulator. Image source: Compact lithium niobate electro-optic modulators, A. Rao, IEEE Journal of Selected Topics in Quantum Electronics, 2018..... 11

Figure 3.1: (a) Waveguide in bulk LN, made through a diffusion process. (b) Diffused waveguide in thin film LN. (c) Rib-loaded waveguide using a combination of LN with another material. (d) Dry-etched LN waveguide. (e) Wafer-bonded LN on SOI waveguide. (f) Silicon waveguide on bulk LN. (g) Silicon substrate, with mechanically thinned LN, bonded by an adhesive. Image source: Compact lithium niobate electro-optic modulators, A. Rao, IEEE Journal of Selected Topics in Quantum Electronics, 2018. 23

Figure 4.1: Cross-section of mechanically thinned $LiNbO_3$ phase modulator. Image source: Thin $LiNbO_3$ on insulator electro-optic modulator, Optics Letters, Andrew Mercante, 2016..... 26

Figure 4.2: Input and output voltage trace, resulting from testing mechanically thinned modulator at 976 nm wavelength..... 27

Figure 4.3: Plot of $V_{\pi,45^\circ}$ vs wavelength. 28

Figure 5.1: Fabrication of phase modulator by direct wafer-bonding. (a) Starting wafer, 200 nm SiN on Quartz. (b) SiN is etched into ridge waveguide. (c) Second wafer, LN on Si, is inverted. (d) Second wafer is bonded onto the first wafer. 30

Figure 5.2: Processing of hybrid SiN/LN sample after wafer-bonding. (a) Cross-section after wafer-bonding. (b) Si and SiO_2 layers are removed by etching. (c) Au electrodes are formed in contact with the LN layer. 30

Figure 5.3: Three different simulations of wafer-bonded hybrid SiN/LN waveguide. Thickness of LN layer is 300 nm; width of SiN ridge is 800 nm; thickness of SiN ridge is varied. 31

Figure 5.4: Simulations of SiN on Qz waveguide; second and third columns show simulations of under-etching..... 32

Figure 5.5: Simulations of SiN on Qz waveguide, showing over-etching. 33

Figure 5.6: Wafer-bonding with adhesive materials. (a) Wafer-bonding with BCB. (b) Wafer-bonding with gold. 34

Figure 5.7: Optical simulation of waveguide, at 1064 nm, with 300 nm thick layer of BCB..... 34

Figure 5.8: Simulations of wafer-bonded LN/SiN waveguide with gold. (a) TE mode plot with 6 μm gap. (b) Plot of optical loss versus electrode gap. 35

Figure 5.9: Three-dimensional visualization of wafer-bonding procedure with gold**.** 36

Figure 6.1: Schematic of $LiNbO_3$ phase modulator with etched LN ridge waveguide. 37

Figure 6.2: Cross-section diagram of $LiNbO_3$ phase modulator. Inset shows mode plot of the TE optical mode, resulting from the simulation in Lumerical MODE Solutions. 39

Figure 6.3: Simulations of LN ridge waveguide, at 1064 nm, varying the size of the electrode gap. 40

Figure 6.4: Fabrication schematic of low-frequency phase modulator. 41

Figure 6.5: Voltage signals resulting from electro-optic modulator characterization. 42

Figure 7.1: Hybrid SiN/TFLN modulator. (a) Cross-section of modulator. (b) TE mode plot resulting from simulation. 45

Figure 7.2: Simulation of optical loss versus electrode gap for hybrid SiN/LN device. 45

Figure 7.3: (a) Diagram of GSG CPW electrodes. (b) Plot of characteristic impedance vs frequency for the probe region of the electrodes……46

Figure 7.4: (a) Cross-section of GSG CPW electrodes. (b) Simulated results of n_{RF} as a function of frequency. 47

Figure 7.5: Simulated RF electric field distribution for hybrid SiN/LN device. In the simulation, 1 V is applied from signal to ground..... 48

Figure 7.6: Fabrication schematic of high-frequency hybrid SiN/TFLN modulator. . 49

Figure 7.7: Electrode fabrication procedure. (a) Hybrid SiN/TFLN ridge waveguide. (b) Deposition of Ti/Au/Ti seed layer. (c) Photoresist spin-coating. (d) Sample after exposure and developing. (e) Electrodes are built up by electroplating. (f) Photoresist removal. (g) Removal of top Ti layer. (h) Removal of Au layer. (i) Removal of bottom Ti layer. 51

Figure 7.8: Measured S-parameters of electrodes in high-frequency modulator. 52

Figure 7.9: Overall loss of GSG CPW electrodes as a function of frequency, with curve fit. 53

Figure 8.1: Schematic of intensity modulator. 54

Figure 8.2: Results of simulation of cross-sections of MMI. In the region of 0.5 μm width, one mode was found. In the region of 1.3 μm width, four modes were found. This is desirable for 1×2 MMI operation..... 55

Figure 8.3: Diagram of multi-mode interference (MMI) coupler. (a) MMI with tapered input and two tapered outputs. (b) MMI with non-tapered input and two tapered outputs. 56

Figure 9.1: Schematic of analog photonic link system..... 59

Figure 9.2: Schematic of single-pixel mmW Antenna system. 60

Figure 9.3: Spectra of optical signals in mmW imaging system. (a) Spectrum of optical signal after exiting phase modulator. (b) Dashed line indicates effect of filter. (c) Spectrum of optical signal after the filter. 61

ABSTRACT

Across the world, the telecommunications industry has deployed numerous systems for rapid transmission of data across long distances, including cell phone and internet networks. Photonic technologies and fiber-optic communications are ubiquitous in these systems because they allow for lower loss and greater energy efficiency than a conventional electrical transmission line. One photonic device that is crucial to these systems is the electro-optic modulator, which converts signals from the electrical domain to the optical domain at high speed.

Lithium niobate is the material of choice for electro-optic modulators and many such devices have been demonstrated, in bulk lithium niobate at 1550 nm and 1064 nm, as well as thin-film-lithium-niobate (TFLN) at 1550 nm. This thesis presents the first analysis of electro-optic modulators in thin-film-lithium-niobate at shorter wavelengths, especially 1064 nm. Since the half-wave voltage (V_π) is proportional to the wavelength, a modulator at 1064 nm has the notable advantage of a lower V_π compared to a similar modulator at 1550 nm. Another significant advantage can be identified when considering the modulator as a component in a larger photonic system, such as an analog photonic link system or an imaging system. In such a system, the modulator would be used in conjunction with light-sensing components (photodetectors and/or image sensors). At 1550 nm, the light-sensing components must be made of III-V semiconductor materials, which are more expensive. However, a system implemented at 1064 nm can use silicon light-sensing components, which are available at lower cost and are CMOS-compatible.

Thus, the modulators presented in this thesis open the door towards photonic systems in which the overall cost is reduced.

Chapter 1

INTRODUCTION

1.1 Electro-optic modulators

Electro-optic modulators have been in use for nearly six decades, with applications in long-haul telecommunication networks [1], optical quantum memories [2], RF photonics [3], millimeter-wave (mmW) imaging systems [4], and communication within data centers [5]. Within the telecommunications industry, there is a constant desire for higher data rates and higher frequencies. One of the more recent trends is for modulators to be made from thin-film-lithium-niobate, instead of bulk lithium niobate. This has been demonstrated at the 1550 nm wavelength, which is the most commonly used wavelength in telecommunications due to its low absorption in optical fibers. But, prior to this work, thin-film-lithium-niobate (TFLN) modulators have not been demonstrated at the 1064 nm wavelength.

Existing publications have demonstrated bulk $LiNbO_3$ modulators at 1550 nm, and these are available as commercial-off-the-shelf (COTS) devices, such as the modulators shown in Figure 1.1. Bulk $LiNbO_3$ modulators at 1064 nm are also in existence as COTS devices and they find their applications in optical interconnects [6], frequency comb generation [7], and free-space optical (FSO) communications [8]. In research publications, there have also been thin-film-lithium-niobate (TFLN) modulators at 1550 nm, which are applicable to long-haul telecommunications. Presented in this

work are the first devices, to the best of our knowledge, that combine the 1064 nm wavelength with the TFLN platform.

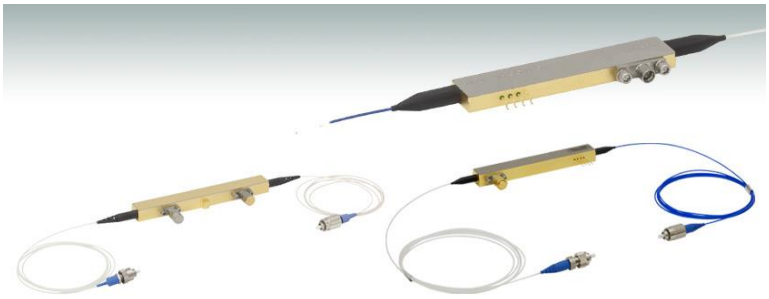

Figure 1.1: Commercial-off-the-shelf (COTS) electro-optic modulators. Image source: ThorLabs.com.

1.2 Analog photonic link systems

The application of combining photonic devices in an analog link system has been studied for many years, with ongoing research into the present day. Such a system typically includes an electro-optic modulator, a laser as an optical source, an electrical source applied to the modulator, optical fibers, and one or more photodetectors. Work on analog photonic links often focuses on enhancing the spurious-free dynamic range (SFDR) of a link [9] or suppressing the third-order intermodulation distortion (IMD3) [10]. The devices presented in this work could be used as part of a link system with an operating wavelength of 1064 nm. This is discussed further in Chapter 9.

1.3 Millimeter-wave imaging systems

While there are a number of ways of imaging millimeter waves (mmW), one emerging technique is through optical up-conversion. In such a system, mmW's are received by an antenna that outputs a voltage signal, which is then applied to the electrodes of an electro-optic modulator. The result is that the output of the modulator contains sidebands that carry the information from the incident mmW. These sidebands can then be filtered and detected by a photodetector. Such a system has already been implemented at the 1550 nm wavelength [3]. Variations of this have also been implemented where the system contains not just one, but multiple antennas forming an array. The construction of a single antenna mmW imaging system, at the 1064 nm wavelength, is discussed in Chapter 9.

Chapter 2

ELECTRO-OPTIC MODULATOR FUNDAMENTALS

2.1 Low-Frequency Operation

An electro-optic modulator is typically used along with a laser, which passes through the modulator and, simultaneously, a voltage is applied to the modulator's electrodes, thereby causing modulation of the light. The modulators discussed in this thesis are all based on the Pockels effect, which means that the refractive index, *n*, of the material changes in response to an applied electric field, *E*:

$$n(E) = n - \frac{1}{2} r n^3 E. \tag{2.1}$$

The coefficient *r* is called the Pockels coefficient. In terms of impermeability, $\eta = 1/n^2 = 1/\varepsilon_r$, the equation can be written as:

$$\eta(E) \approx \eta + rE. \tag{2.2}$$

As a result of this change in refractive index and impermeability, there is a corresponding phase shift of light traveling through the modulator:

$$\Delta\phi = \phi_0 - \pi \frac{r n^3 E L}{\lambda_0}, \tag{2.3}$$

where ϕ_0 is the initial phase of the light as it enters the modulator, *L* is the length of the interaction region, and λ_0 is the free-space wavelength. Lithium niobate is widely used for such modulators because it exhibits a strong Pockels effect. It is a crystalline compound of lithium, niobium, and oxygen that exhibits many desirable properties, including a wide transmission spectrum, high extinction ratio, low third-order susceptibility, and superior temperature stability. Because lithium niobate is a crystal, it is

optically anisotropic. A full description of the electro-optic properties requires the use of tensors:

$$\eta_{ij}(E) = \eta_{ij} + \sum_k r_{ijk} E_k. \tag{2.4}$$

This equation is analogous to equation 2.1; η_{ij} is the impermeability tensor, r_{ijk} is an electro-optic tensor with 27 coefficients, and E_k represents the three components of the electric field vector.

Lithium niobate is a uniaxial crystal, and can therefore be described by two different values of refractive index, n_o (ordinary) and n_e (extraordinary). It is helpful to consider two components of the electro-optic tensor, r_{13} and r_{33}, which correspond to n_o and n_e respectively. Nearly all electro-optic modulators include an optical waveguide, consisting entirely or partially of lithium niobate, thus forming an anisotropic waveguide. In such a waveguide, there are two optical modes (TE mode and TM mode) and each experiences a phase shift independent of the other, which can be described as [15]: (2.5)

$$\Delta\phi_h = \frac{\pi}{\lambda} n_e^3 r_{33} \Gamma \frac{V}{d} L,$$

and

$$\Delta\phi_v = \frac{\pi}{\lambda} n_o^3 r_{13} \Gamma \frac{V}{d} L, \tag{2.6}$$

where V is the applied voltage and d is the gap between the electrodes. Γ is the mode overlap integral parameter and represents how much the modulating electric field overlaps with the optical field. It is given by:

$$\Gamma = \frac{1}{V} \frac{\iint \frac{1}{2} n_e^3 r_{33}(z,x) E_m(z,x) |E_o(z,x)|^2 \, dS}{\iint |E_o(z,x)|^2 \, dS}, \tag{2.7}$$

where E_m is the modulating electric field, E_o is the electric field associated with the optical mode, and V is the applied voltage required to produce E_m. The equation above assumes an *x*-cut LN device, where the light is *y*-propagating, and thus *z* and *x* are the axes in the plane perpendicular to the direction of propagation.

The half-wave voltage (V_π) is a commonly used figure of merit (FOM) for electro-optic modulators and represents the amount of voltage required to induce a phase shift of π radians. An isotropic modulator would have a single value of V_π, but the anisotropic lithium niobate modulators described in this work have two different values of V_π, corresponding to the two optical modes in the waveguide. The half-wave voltage associated with the TE mode is:

$$V_{\pi,TE} = \frac{\lambda_0 d}{(n_e^3 r_{33})\Gamma L}, \tag{2.8}$$

and the half-wave voltage associated with the TM mode is:

$$V_{\pi,TM} = \frac{\lambda_0 d}{(n_o^3 r_{13})\Gamma L}. \tag{2.9}$$

These are derived from Equations 2.4 and 2.5 by setting the phase shift equal to π radians.

For an anisotropic waveguide, it is common to use a polarization rotation method to measure the half-wave voltage at 45 degrees ($V_{\pi,45^\circ}$), which is a well-established technique [18], [26], [30], [32]. A number of measurements of $V_{\pi,45^\circ}$ are reported in this thesis and they are all obtained using the setup shown in Figure 2.1(a). Light from a laser is fed into the modulator, using a polarization-maintaining single-mode lensed fiber

aligned to the entrance facet. This fiber is keyed and rotated so that the light is linearly polarized at +45° from the horizontal (Figure 2.1(b)).

Simultaneously, a 1 kHz sawtooth voltage signal (V_{in}) is applied to the electrodes of the device, from a function generator. In order to apply this signal to the microscopic electrodes on our devices, a micropositioner (Signatone Model S-926) is used, along with a magnetic base (ThorLabs MB175) and a tungsten probe tip (Signatone SE-10T). First, a microscope camera is positioned so that the electrode is in view. Then the probe tip is moved to a position slightly above the electrode, aligned to the electrodes in the *x* and *y* direction. It appears as a silhouette because it is slightly out of focus. Next, the micropositioner is used to bring the tip down, in the *z* direction. As it contacts the electrode, it comes into focus and slides a few microns across the wafer, which confirms that electrical contact has been made.

The light exiting the modulator is elliptically polarized (Figure 2.1(c)), due to the unequal phase shift of the TE and TM modes within the modulator's waveguide. This light is collected by a second lensed fiber, identical to the first one, aligned to the modulator's exit facet. After passing through this fiber, the light passes through a linear polarizer (LP) (ThorLabs ILP1064PM-FC), which is oriented so that its transmission axis is at –45° from the horizontal (Figure 2.1(d)). This polarizer extracts a component of the elliptically polarized light, resulting in intensity modulation of the light exiting the LP. This is received by a silicon photodetector (Si PD), which produces a current proportional to the light intensity. All $V_{\pi,45^\circ}$ measurements described in this thesis are performed at CMOS-compatible wavelengths, i.e. ~1 μm, and thus they can be done with a silicon

photodetector (ThorLabs DET02AFC), which is available at lower cost than a III-V detector. The setup in Figure 2.1 serves as an example of a system where the total cost of assembly is reduced. The current produced by the PD flows into a transimpedance amplifier (TIA) (DHPCA-100), which produces a voltage signal (V_{out}).

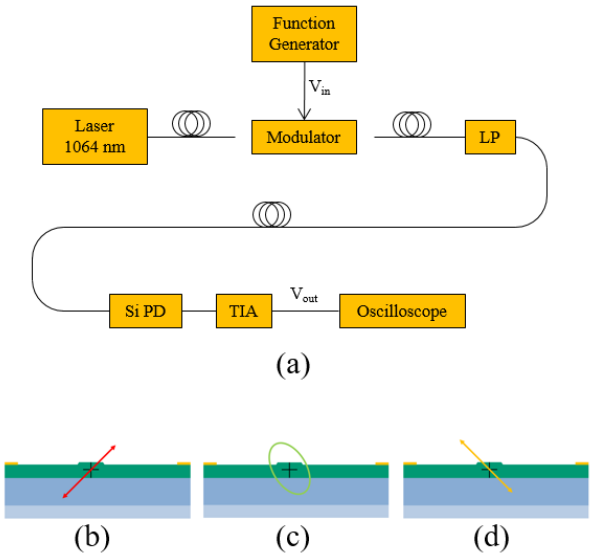

Figure 2.1: (a) Experimental setup for low-frequency characterization of phase modulator and measurement of $V_{\pi,45°}$. (b) Linearly polarized light, at +45°, at the entrance facet of the modulator. (c) Elliptically polarized light at the exit facet of the modulator. (d) Orientation of the axis of the linear polarizer (LP).

The voltage signals V_{in} and V_{out} are displayed together on an oscilloscope and exported. Within the V_{out} signal, a minimum and its nearest maximum are identified. The shift in V_{in} that corresponds to these two points is $V_{\pi,45°}$ or the half-wave voltage at 45 degrees. This is the voltage that causes the exiting light to shift from +45° to –45° polarization. The difference between the horizontal phase shift and the vertical phase shift is:

$$\Delta\phi = \Delta\phi_h - \Delta\phi_v = \frac{\pi}{\lambda_0}(n_e^3 r_{33} - n_o^3 r_{13})\Gamma\frac{V}{d}L. \quad (2.8)$$

By setting this difference equal to π radians and solving for voltage, an equation for $V_{\pi,45}$ is found:

$$V_{\pi,45^\circ} = \frac{\lambda_0 d}{(n_e^3 r_{33} - n_o^3 r_{13})\Gamma L}. \quad (2.9)$$

Combining equations 2.7 and 2.9 and using n_e = 2.1555, n_o = 2.2321, r_{33} = 32.2 pm/V, and r_{13} = 10 pm/V gives:

$$V_{\pi,TE} = \frac{n_e^3 r_{33} - n_o^3 r_{13}}{n_e^3 r_{33}} V_{\pi,45^\circ} = .655 V_{\pi,45^\circ}, \quad (2.10)$$

which is a helpful relation in an experimental setting. The intended use for all devices described herein is with light traveling in the TE mode only, which is achieved by feeding horizontally polarized light into the entrance facet, and therefore $V_{\pi,TE}$ is the more important figure of merit.

Every modulator has optical loss, with the overall insertion loss consisting of coupling loss and propagation loss. Coupling loss refers to the loss that occurs when light exits the fiber and enters the waveguide facet. It depends on the quality of the waveguide facet, as well as the mode overlap between the fiber mode and the waveguide mode. Meanwhile, propagation loss occurs as the light travels through the waveguide. Propagation loss includes metal-induced absorption loss resulting from the optical mode overlapping with the metal electrodes, scattering loss due to sidewall roughness, as well as the inherent material absorption of the LN and other materials making up the waveguide.

In order to assess the amount of coupling loss and the amount of propagation loss, it is common to perform a cutback measurement. In this type of measurement, samples are prepared with waveguides of varying lengths. The overall optical loss is measured for each waveguide, and these values in dB can be subtracted and divided by the difference in waveguide length to compute the propagation loss per unit length, in dB/cm. This dB/cm value can be used for a more thorough analysis, separating the loss into propagation loss and coupling loss.

The gap between the electrodes (*d* in the equations above) is an important parameter and must be chosen carefully based on optical simulations. There is an inherent tradeoff; a smaller electrode gap results in a lower V_π, but also results in greater metal-induced absorption loss. If the waveguide has a more tightly confined optical mode, then the electrode gap can be smaller, resulting in a higher electric field per volt and lower V_π. Decreasing the gap further, beyond a certain value, will always result in significant metal-induced loss, which is unacceptable for a real device. Different waveguide structures will have different values of the critical electrode gap.

The discussion above refers to a phase modulator, illustrated in Figure 2.2(a)). However, intensity modulators are also useful devices. The most common type of intensity modulator is a Mach-Zehnder Modulator (MZM), which operates by splitting the incoming light into two paths or arms, as seen in Figure 2.2(b). The phase of the light is shifted along one or both paths. Subsequently, the light from the two paths is re-combined into one path, wherein it experiences either destructive interference or constructive interference, depending on the phase shift. The amount of phase shift

depends on the voltage and, thus, the output light may have low intensity or high intensity depending on the applied voltage. Destructive interference occurs when the phase shift in one arm is π radians; therefore the half-wave voltage, V_π, is the voltage required to switch an MZM between its on and off states.

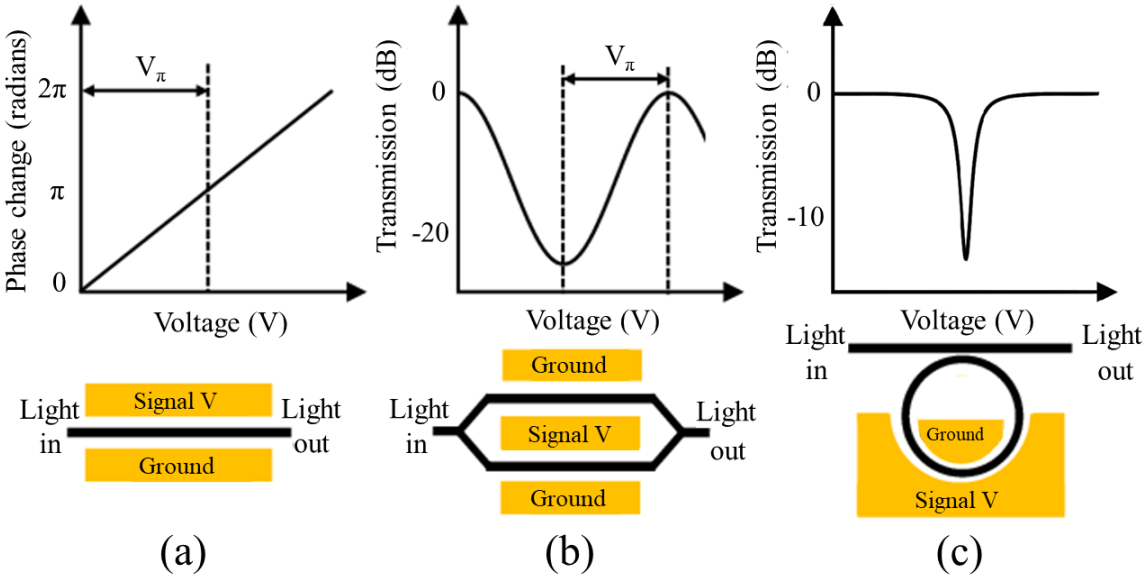

Figure 2.2: (a) Electro-optic phase modulator. (b) Mach-Zehnder intensity modulator. (c) Microring modulator. Image source: Compact lithium niobate electro-optic modulators, A. Rao, IEEE Journal of Selected Topics in Quantum Electronics, 2018.

Ideally, in an intensity modulator, the input light is split equally and 50% of the optical power ends up in each arm. With this assumption, the intensity of the output light is:

$$I_o = \frac{1}{2} I_i + \frac{1}{2} I_i \cos\phi = I_i cos^2(\phi/2). \qquad (2.11)$$

However, in practice, a perfect 50-50 split is not possible, and loss occurs during splitting. Therefore, a non-ideal split may occur, for example, 47% of the optical power may end up in one arm and 53% in the other arm. As a result, the light does not

experience perfect destructive interference when it recombines, and it is therefore not possible for the output light intensity to be exactly zero in a real device. Accordingly, the power of the output light will have some minimum value, which is orders of magnitude smaller than its maximum value. The ratio of the optical power at maximum and minimum transmission is the optical extinction ratio (OER), usually expressed in dB. An ideal MZM has infinite OER, but the non-ideal properties mentioned above result in a finite OER.

Although not the focus of this thesis, the microring modulator is another important type of modulator, shown in Figure 2.2(c). This type of modulator consists of a set of two waveguides, where one is straight, and the other is a closed loop. Light is input into the straight waveguide and coupling occurs from the straight waveguide to the loop because of their proximity. Light builds up in intensity over multiple round trips through the ring due to constructive interference. In the absence of electrodes, this is known as an optical ring resonator. When electrodes are included adjacent to the ring, the device becomes a tunable ring resonator, or a microring modulator. The voltage applied to these electrodes can then be used to control the amount of light transmission through the device. There will be a particular value of voltage for which the transmission drops to a minimum, as seen in the graph in Figure 2.2(c).

2.2 High-Frequency Operation

When the wavelength of the modulating voltage signal is long compared to the length of the device's electrodes, L, the device is said to be operating at low frequency.

This occurs when $L<<10\lambda$, and the lumped-element model is used. When this wavelength becomes comparable to L, the device is said to be operating at high frequency. Bulk LN devices have been demonstrated that operate up to 300 GHz [4], and thin-film LN devices have been shown to operate up to 500 GHz [26].

When designing an electro-optic modulator to operate at such high frequencies, there are additional considerations. For such a modulator, there are typically three electrodes, forming a ground-signal-ground coplanar waveguide (GSG CPW) transmission line, with voltage traveling through the electrodes as a radio frequency (RF) wave. The RF wave and the optical wave co-propagate through the device, and this is described as a traveling-wave modulator. The electric field associated with the RF wave is described by:

$$E_z(f_m, y, t) = E_0 e^{-\alpha(f_m)y} e^{j2\pi f_m t}, \tag{2.12}$$

where f_m is the frequency of the modulating signal, and α is the propagation loss, which depends on frequency. It is assumed that the RF wave propagates along the y-axis, and its electric field only includes a z-component.

For the greatest modulation efficiency, the RF wave and the optical wave must travel at the same speed and with the same dielectric constant. Ideally, the group velocity of the optical waveguide must be matched to the phase velocity of the RF waveguide. Thus, it is necessary to perform index matching between n_{opt} and n_{RF}, where n_{opt} is the optical group index and n_{RF} is the RF phase index, where $n = \sqrt{\epsilon_r}$. This can be a challenge because LN exhibits significant variation in its refractive index at different frequencies; its RF refractive index is around 6.6, but its optical refractive index is around

2.2. For bulk LN devices, n_{RF} is greater than n_{opt}, and this index matching is achieved by lowering n_{RF}. To do this, electrodes can be fabricated at a significant thickness (up to 30 μm thick), ribs can be etched into the LN, and SiO_2 buffer layers can be added, all of which serve to reconfigure the modulating electric field, so that less of it passes through the LN [4]. This reconfiguration comes with a disadvantage, because it has the undesirable side effect of reducing the overlap between the RF mode and the optical mode, which increases the half-wave voltage and decreases conversion efficiency.

Meanwhile, thin-film LN devices have the opposite problem, where n_{RF} lower is lower than n_{opt} by default. Most of the RF field passes through the handle, which may be silicon or quartz. Therefore, to achieve index matching in thin-film devices, the n_{RF} must be increased. A proven method in the literature for increasing n_{RF} is by cladding the modulator with a high-index material such as UV15 adhesive, which has an RF index near 1.73 [28].

Measurement of the electrodes of a high-frequency modulator is typically done with a Performance Network Analyzer (PNA), which directly measures the two-port scattering parameters (*S*-parameters) by applying a high-frequency voltage signal and measuring the transmission and reflection. From the *S*-parameter measurement, it is possible to determine the 3 dB cutoff frequency and maximum operating frequency. Along with this PNA measurement, software is used to calculate loss due to metal conductivity (α_{m0}), dielectric loss (α_{d0}), effective RF index (n_{RF}), and impedance (Z_{m0}).

Furthermore, an Optical Spectrum Analyzer (OSA) (Yokogawa AQ6319) is used to detect sidebands in the modulator's optical output. The optical modulation spectrum is

measured, which will typically include the carrier, upper sideband, lower sideband, and harmonics. In addition to the OSA and the modulator, an optical source (laser) and a signal generator (PNA) are required. The PNA will typically have a maximum frequency in its default configuration and thus range extenders are used to allow for testing up to higher frequencies.

The half-wave voltage can be measured at low frequencies through the polarization rotation technique described above. However, this technique is not feasible at higher frequencies because it is rare to find COTS photodetectors operating above 10 GHz. Instead, the half-wave voltage can be calculated at high frequencies based on the optical modulation spectrum, using the following equation:

$$V_\pi = \sqrt{\frac{\pi^2 Z_m}{2\eta_{mod}}}, \tag{2.13}$$

where Z_m is the characteristic impedance of the transmission line, and η_{mod} is the modulation efficiency, which may be found as:

$$\eta_{mod} = \frac{I_{FSB}}{I_0 I_m}, \tag{2.14}$$

where I_{FSB} is the power of the first set of sidebands, I_0 is the power of the optical carrier, and I_m is the power of the applied modulating signal.

For high-frequency operation, it becomes necessary to design the electrodes with three regions, a probe region, a taper region, and an interaction region. It is appropriate to simulate the impedance of the probe region, to make sure there is good impedance matching between the 50 Ω probes and the electrodes. Meanwhile, n_{RF} of the interaction region can be found through simulations, which is useful for index matching.

The RF loss over the length of the GSG CPW, $\alpha(f_m)$ in Equation 2.12, is particularly important. The electrode must support the RF mode across its entire length, in order to achieve broadband efficiency. There are three significant loss mechanisms, as shown in the following equation:

$$\alpha(f_m) = \alpha_c\sqrt{f_m} + \alpha_d f_m + \alpha_r f_m^3, \tag{2.15}$$

where α is the overall frequency-dependent loss associated with the GSG CPW, α_c is a coefficient associated with the conduction loss, α_d is a coefficient associated with the dielectric loss, and α_r is a coefficient associated with radiation loss. The units of f_m, $\alpha(f_m)$, α_c, α_d, and α_r are GHz, dB/cm, dB/(cm•GHz$^{1/2}$), dB/(cm•GHz), and dB/(cm•GHz^3). Conduction loss is energy lost as heat in the conductive metal. Dielectric loss results from the electric field passing through the surrounding dielectric material, which causes energy to be lost to heating the dielectric. Radiation loss results from the wave radiating its energy into the substrate as it propagates. At frequencies less than 300 GHz, radiation loss is negligible; conduction loss and dielectric loss are the significant effects.

2.3 System integration

When a modulator operating at 1064 nm is integrated as part of a photonic system, there are a few notable advantages. The first advantage is the reduced half-wave voltage. Since half-wave voltage is proportional to wavelength, a system implemented at 1064 nm will have a lower half-wave voltage compared to a similar system implemented at 1550 nm. This is a metric of the efficiency of the electrical-to-optical conversion. In an

RF photonic link system, a modulator with a lower half-wave voltage results in a lower noise figure, higher gain, and lower spurious-free dynamic range (SFDR).

Another advantage becomes clear when considering the light-sensing components within the photonic system. For an analog photonic link system, one or more photodetectors would be used. In a system implemented at 1064 nm, this photodetector would be silicon-based, but in a system that uses 1550 nm, the photodetector would be based on a III-V semiconductor material. The silicon photodetector would be available at a lower cost than the III-V photodetector, thereby reducing the overall cost of the system. Similarly, a photonic millimeter-wave imaging system could be implemented at 1064 nm, and this system would use an array of antennas combined with an image sensor. This image sensor would be Si-based and CMOS-compatible and, again, available at a lower cost than a III-V image sensor.

Chapter 3

BACKGROUND AND LITERATURE OVERVIEW

3.1 Choice of Materials for Electro-optic Modulators

$LiNbO_3$ is the most widely used material for electro-optic modulators, but it is worth noting that other materials have been used. Modulators can be made entirely of silicon, but these have undesirable properties, such as intrinsic absorption loss and low extinction ratio [11] and also lower optical power levels. The integration of silicon with organic materials has been pursued, but such devices are unlikely to be stable in the long term [12]. Modulators have been fabricated based on indium phosphide (InP), and these can achieve high digital data rates, but their intrinsic nonlinearity and material loss is a disadvantage [13]. Barium titanate ($BaTiO_3$) has been demonstrated with an ultra-high electro-optic coefficient, but its high-frequency operation is limited by the large dielectric constant of $BaTiO_3$ (>100) [14]. Among all these materials, $LiNbO_3$ has truly been the most widely used material within the space of long-haul telecommunications, because of its many desirable properties, including a wide transmission spectrum, high extinction ratio, low third-order susceptibility, and superior temperature stability [15]. $LiNbO_3$ enables the fabrication of devices with high data bandwidth and excellent signal fidelity.

3.2 Bulk Lithium Niobate

$LiNbO_3$ modulators can be broken down into two sub-categories, bulk lithium niobate and thin-film lithium niobate. As early as 1982, waveguides were fabricated in

bulk lithium niobate, by means of proton exchange and titanium in-diffusion [16], and this technology was used to produce modulators (Figure 3.1(a)). In proton exchange, lithium ions (Li^+) in the crystal lattice are replaced with hydrogen ions (H^+) in a particular region, increasing the refractive index. In titanium in-diffusion, a strip of Ti is first deposited onto the LN substrate, and then the sample is heated for a few hours, allowing titanium ions to penetrate into the bulk LN. The technology has progressed to the point where today, many COTS bulk LN modulators are available on the market. Most of these devices are designed to operate at the 1550 nm wavelength, but there is also a significant subset that operate at 1064 nm. These bulk LN waveguides at 1064 nm have been used to achieve frequency doubling of 1064 nm light [21]. As discussed in Chapter 2, the half-wave voltage (V_π) of an electro-optic modulator is proportional to the wavelength (λ_0) of the light passing through it, which means that a modulator operating at 1064 nm has the notable advantage of a lower V_π compared to a similar modulator at 1550 nm.

3.3 Thin-Film Lithium Niobate

In 1998, processes were invented to produce thin-films of LN [18]. By 2005, thin-film LN modulators started to appear as an alternative to bulk LN modulators [19], in published literature but not as COTS devices. The transition from bulk LN to thin-film LN reduces V_π [20], due to a smaller optical mode size and more closely spaced electrodes, and this corresponds to a higher electro-optic modulation efficiency. Additionally, thin-film LN devices are more suitable for integration into photonic

integrated circuits (PICs) because of their smaller size and smaller bending radii. Furthermore, thin-film LN devices exhibit a linear voltage–index relationship. They also exhibit wider operational bandwidth, lower drive power, and higher extinction ratio, compared to their bulk LN counterparts. Progress has been made towards the improvement of thin-film LN devices, including the reduction of thermal drift and DC drift [19], and research on thin-film LN modulators has continued up into the present day, almost entirely focused on the 1550 nm wavelength [20-26].

The most important method for producing thin-films of lithium niobate is crystal-ion-slicing (CIS). At least three companies, NanoLN, Partow Technologies LLC, and SRICO, sell TFLN wafers, with multiple wafer sizes and multiple thicknesses of the LN layer. In the CIS technique, a bulk LN sample is bombarded with helium (He^+) ions, which embed themselves in the sample at a given depth and break bonds in the crystal lattice. The depth of implantation determines the final thickness of the film; it can range from 10 nm to 1 μm. A damaged layer exists at the depth where bonds are broken. After this implantation, the wafer is bonded to a handle, typically quartz. Then the sample is annealed, and a thin layer of LN can be exfoliated from the bulk LN sample.

CIS comes with a few disadvantages; first, the implantation of He^+ ions requires expensive equipment. Secondly, this implantation may damage the crystal structure, which means that the sample must be annealed at a high temperature to repair the damage; and thus the process is not considered CMOS-compatible. As an alternative to CIS, LN thin-films may be produced by mechanical thinning, which is a low-temperature process; this is discussed in more detail below. Additionally, thin-films of LN can be

produced by other methods including sputtering, dicing, vapor phase transport, liquid phase epitaxy, and sol-gel processing, but all of these are less commonly used.

Thin-film lithium niobate waveguides are fabricated in a number of different ways, as shown in Figure 3.1. It is possible to perform diffused proton-exchange in thin-film LN, as shown in Figure 3.1(b). The technique is similar to proton-exchange in bulk LN, but the mode size is smaller; a mode as small as 0.6 μm^2 has been found in simulation, and mode sizes have been measured to be 3.3 μm^2 by measurement of near-field intensity distribution [37]. This can be done at low cost compared to other methods, and the technology is mature because it has already been used for many years in bulk LN.

As an alternative to proton-exchange, a different material such as SiN can be deposited onto the thin-film LN; this is known as a rib-loaded waveguide or a strip-loaded waveguide (Figure 3.1(c)). Researchers have actively explored this rib-loaded structure, which is essentially an example of hybrid integration of LN with another material. In fact, a variety of photonic devices have been fabricated based on this hybrid platform: not just phase modulators, but also wavelength converters, tunable micro-ring resonators, mid-infrared modulators, and Mach–Zehnder modulators. The refractive index of the rib-loading material must be closely matched to that of the LN. Some examples of materials used with LN are silicon (Si), tantalum pentoxide (Ta_2O_5), titanium dioxide (TiO_2), chalcogenides (ChG), and silicon nitride (SiN). Among these materials, SiN is the best choice, because it is compatible with photonic integrated circuits (PICs), its refractive index is close to that of LN, it has low second-order nonlinearity, its propagation loss is low, and it is able to handle high optical power. Furthermore, it is

transparent in the visible-NIR and beyond, it does not suffer from two-photon absorption, and it is suitable for low-cost mass fabrication because it is compatible with CMOS-based processes. Recently, a sub-1-volt V_π modulator was demonstrated at 1550 nm in this in hybrid SiN-LN platform [20].

There are two processes for depositing SiN on LN, low-pressure chemical vapor deposition (LPCVD) and plasma-enhanced chemical vapor deposition (PECVD). When PECVD SiN is used, the process has a higher yield and less risk of damaging the LN layer, but it results in a greater optical loss because of the presence of hydrogen in the SiN. Meanwhile, the LPCVD process has lower optical loss, but it has a lower yield because it can cause cracks in the LN layer due to high temperatures. For the fabrication processes described in this thesis, LPCVD SiN is considered; these are wafers purchased from Mark Optics and NanoLN, and thus the LPCVD is done off-site. It is worth noting that the LPCVD SiN could be replaced with PECVD SiN in all cases; this would enable on-site fabrication at a lower cost.

It is possible to etch the thin-film LN to form a ridge waveguide (Figure 3.1(d)). Dry-etching is preferred over wet-etching, because wet-etching of LN is isotropic, and therefore does not enable the formation of small waveguide cross-sections. Chemical dry-etching is difficult, so researchers have investigated dry-etching assisted by argon, as well as argon milling. Typically, dry-etching of LN results in high propagation loss due to surface roughness. The fabrication of such a device is discussed in Chapter 6.

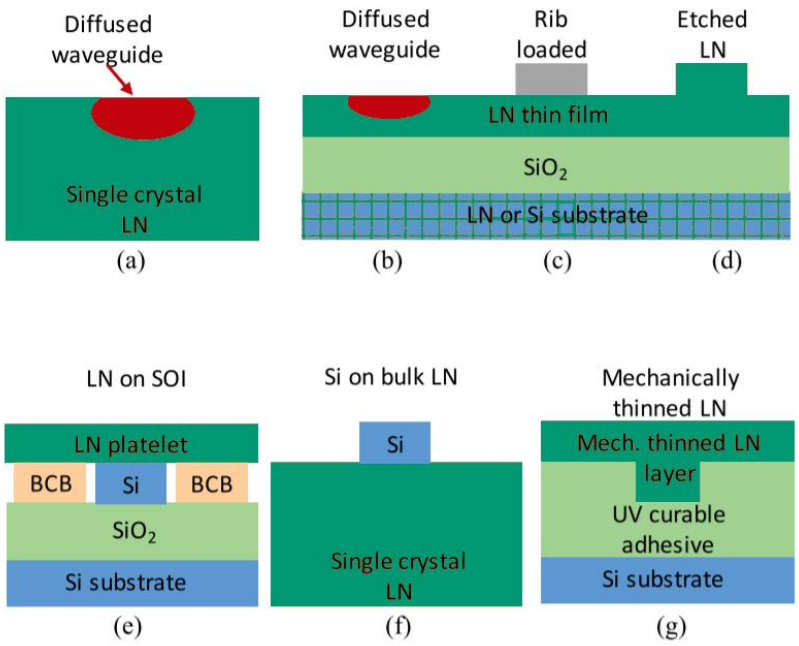

Figure 3.1: (a) Waveguide in bulk LN, made through a diffusion process. (b) Diffused waveguide in thin-film LN. (c) Rib-loaded waveguide using a combination of LN with another material. (d) Dry-etched LN waveguide. (e) Wafer-bonded LN on SOI waveguide. (f) Silicon waveguide on bulk LN. (g) Silicon substrate, with mechanically thinned LN, bonded by an adhesive. Image source: Compact lithium niobate electro-optic modulators, A. Rao, IEEE Journal of Selected Topics in Quantum Electronics, 2018.

Figure 3.1(e) shows wafer-bonding, where a thin-film LN wafer is bonded onto a strip-loaded waveguide structure, such as silicon-on-insulator (SOI) or SiN, using special transfer techniques. One advantage of this technique is that the LN is not etched or processed in any way, and thus the waveguide does not have the surface roughness mentioned in the previous paragraph. However, this wafer-bonding process comes with some challenges; it is difficult to incorporate electrodes, and the handle of the upper wafer may need to be removed. Some of these concerns are addressed in Chapter 5. Furthermore, the fabricated devices may be unreliable. They may also suffer from loss due to a poor mode transition between the SiN waveguide and the hybrid SiN-LN

waveguide; this results from reflections at the interface, differences in mode profiles, and differences in effective indices between the two waveguides.

Figure 3.1(f) shows the Si on LN platform, consisting of a bulk LN substrate with a thin-film of silicon. Amorphous Si can be directly deposited on a LN substrate, and subsequently patterned by dry etching. After patterning, the higher refractive index of silicon provides optical confinement. This is a useful platform for high density integrated optics, and electro-optic tunable micro-ring resonators have been demonstrated in this platform [36].

Figure 3.1(g) shows a mechanically thinned LN waveguide, which is fabricated by thinning down a bulk LN wafer. To achieve this, the first step is to prepare a Si handle and bond it via Crystal Bond adhesive to a glass mounting disc. This stack of Si and glass is inserted into a wafer-bonding unit, which uses vacuum, heat and pressure to intensify the bond and remove any air pockets that were present between the layers. Next, a bulk LN wafer is patterned by dry-etching, and this patterned wafer is bonded to the Si handle wafer, using a UV curable adhesive. Next, thinning is done by lapping the LN layer with Al_2O_3 slurries, and then polishing the LN down with a felt pad and a diamond solution to form the thin-film. Finally, the handle is separated from the glass mounting disc by heating the sample above the melting point of the Crystal Bond. With this technique, it is possible to achieve sub-10 μm thickness, but a sub-micron thickness is not easy to achieve without the use of more expensive equipment.

Prior to this work, thin-film LN waveguides have not been extensively studied at wavelengths in the VNIR (very-near infrared) range, shorter than 1550 nm. This thesis

presents some of the first research performed examining the excitation of thin-film LN waveguides with shorter wavelengths of light, including 1064 nm, 976 nm, and 850 nm. The waveguide platforms of Figure 3.1 (c), (d), (e), and (g) are all addressed, through various simulations and fabricated devices. Switching to a shorter wavelength reduces the half-wave voltage, resulting in greater efficiency. It also opens the door for integration with low-cost silicon detectors.

Chapter 4

ALTERNATE WAVELENGTH MEASUREMENTS OF TFLN MODULATORS

At first, work was focused on one particular TFLN modulator, which had already been fabricated and characterized at 1550 nm. This modulator was fabricated by the mechanical thinning technique as described in Chapter 3, and it uses an inverted-rib optical waveguide structure. The cross-section of this modulator is shown in Figure 4.1, along with the TE optical mode resulting from the simulation. This modulator had already been characterized at 1550 nm and it was found that the $V_{\pi,45^\circ}$ was 13.5 volts.

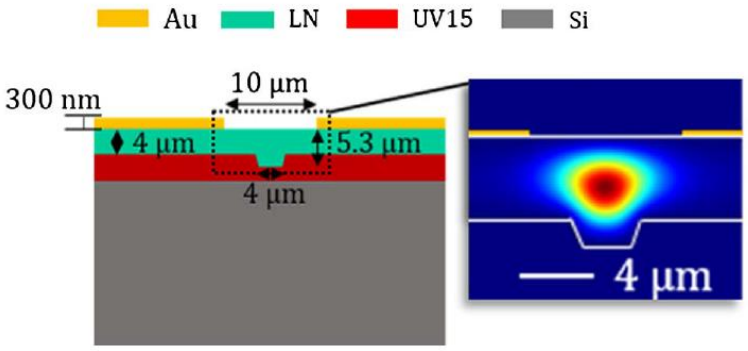

Figure 4.1: Cross-section of mechanically thinned $LiNbO_3$ phase modulator. Image source: Thin $LiNbO_3$ on insulator electro-optic modulator, Optics Letters, Andrew Mercante, 2016

New tests were performed wherein this modulator was characterized with shorter wavelengths of light, at 1064 nm, 976 nm, and 850 nm. In all cases, the half-wave voltage at 45 degrees ($V_{\pi,45^\circ}$) was measured, using the technique described in Chapter 2 and the experimental setup illustrated in Figure 2.1. Using a 1064 nm laser (QPhotonics, QFBGLD-1064-400, 400 mW) and lensed fibers (Oz Optics), the $V_{\pi,45^\circ}$ was measured as 8.5 volts.

At 976 nm, a test performed with cleaved fibers produced a $V_{\pi,45^\circ}$ of 9.2 volts. The voltage traces from this experiment are shown in Figure 4.2. A similar test at 976 with lensed fibers gave a $V_{\pi,45^\circ}$ of 7.0 volts. These two results seem to indicate that the mode overlap integral factor, Γ, is greater when lensed fibers are used (Equation 2.9). In other words, the mode matching is better when lensed fibers are used, as compared to cleaved fibers.

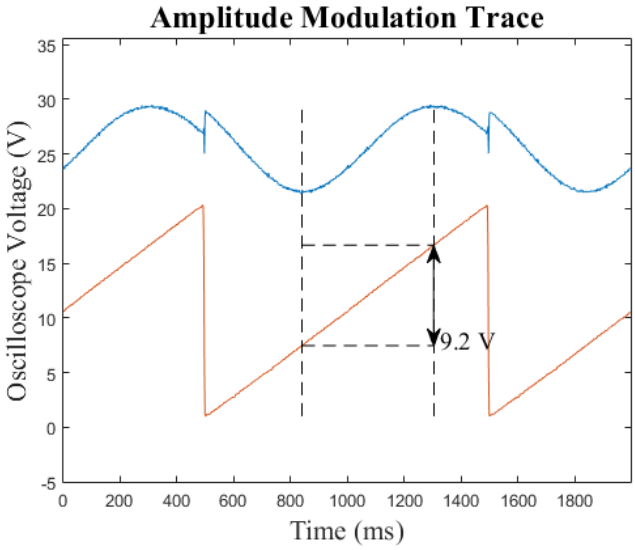

Figure 4.2: Input and output voltage trace, resulting from testing mechanically thinned modulator at 976 nm wavelength.

At 850 nm, with lensed fibers, the $V_{\pi,45^\circ}$ was 6.4 volts. At 850 nm, unusual behavior was observed where the output trace on the oscilloscope was unstable and randomly changing; the conclusion is that the modulator was exhibiting multimode behavior and hopping between modes when used at this wavelength. The value of 6.4 V was determined by freezing the trace and exporting it.

Ignoring the result with the cleaved fibers, and only considering the results with lensed fibers, these measured values of $V_{\pi,45^\circ}$ are consistent with the theory (Equation

2.9), which shows a linear relationship between $V_{\pi,45^\circ}$ and λ_0. A plot is shown in Figure 4.3 with the line of best fit.

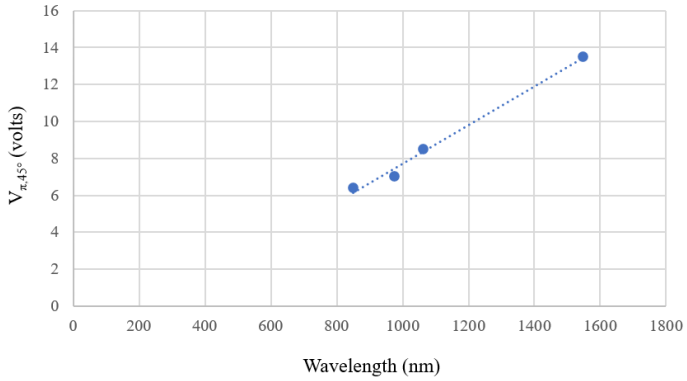

Figure 4.3: Plot of $V_{\pi,45^\circ}$ vs wavelength.

Chapter 5

DESIGN OF WAFER-BONDED PHASE MODULATOR IN TFLN AT 1064 NM

The next objective was to design and fabricate modulators that operate at 1064 nm, with single-mode behavior. Among the wavelengths previously mentioned, 1064 nm was chosen because a hybrid SiN/TFLN modulator was desired, and the 1064 nm wavelength has the lowest absorbance in SiN.

As a starting point, simulations were run of a hybrid SiN/TFLN wafer-bonded modulator. These simulations were based on two types of available wafers. The first type of wafer, procured from Mark Optics, has a 500 μm quartz handle and a thin-film of SiN, whose thickness can be 200 nm, 80 nm, or 40 nm. These SiN thin-films are deposited by means of LPCVD. The second type of wafer is procured from NanoLN and contains a Si handle and a 300 nm layer of X-cut thin-film lithium niobate (TFLN). Between the TFLN and the Si is a bonding layer of silicon dioxide (SiO_2), deposited by PECVD. It is possible to combine these two wafers to produce a wafer-bonded modulator. The proposed fabrication process is shown in Figure 5.1; the silicon nitride is etched into a ridge waveguide, and the lithium niobate wafer is bonded on top of the first wafer.

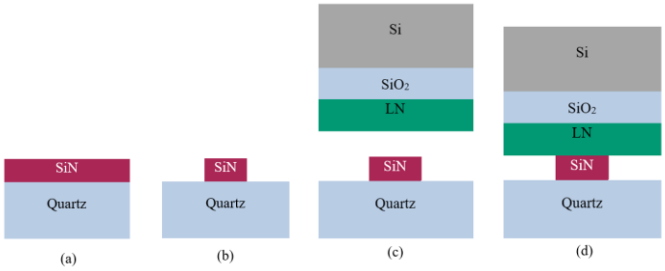

Figure 5.1: Fabrication of phase modulator by direct wafer-bonding. (a) Starting wafer, 200 nm SiN on Quartz. (b) SiN is etched into ridge waveguide. (c) Second wafer, LN on Si, is inverted. (d) Second wafer is bonded onto the first wafer.

In this wafer-bonded waveguide, light can travel in a hybrid mode where it is partially confined in the SiN and partially confined in the TFLN. One possibility is direct wafer-bonding with no adhesive between the two wafers. After direct wafer-bonding, the Si handle and the SiO_2 bonding layer of the upper wafer must be removed, to allow for the formation of electrodes. This is illustrated in Figure 5.2; the handle removal must be done with a selective ICP process that etches Si and SiO_2 but not LN. Once this step is complete, gold electrodes can be formed on top of the LN by electroplating.

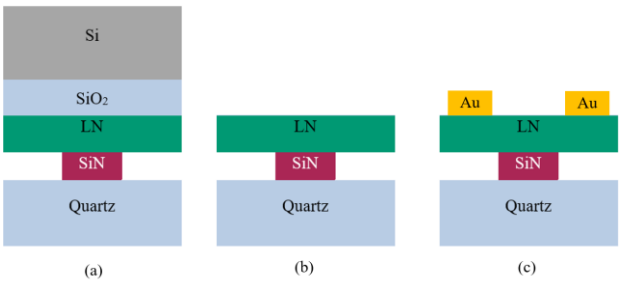

Figure 5.2: Processing of hybrid SiN/LN sample after wafer-bonding. (a) Cross-section after wafer-bonding. (b) Si and SiO_2 layers are removed by etching. (c) Au electrodes are formed in contact with the LN layer.

This structure was simulated in Lumerical Mode Solutions, a solver based on the finite-difference time-domain (FDTD) method, and this resulted in one TE optical mode. In the simulation, the free-space wavelength was 1064 nm, and the optical indices were n_{LNe} = 2.1555, n_{LNo} = 2.2321, n_{SiN} = 1.9861, and n_{Qz} = 1.4494. Figure 5.3 shows three variants of this simulation, in which the thickness of the SiN layer is altered to the three values mentioned above, corresponding to the three available wafers. As the SiN layer becomes thinner, horizontal spreading of the mode is seen. Meanwhile, the mode confinement factor in the LN becomes larger, which increases the electro-optic efficiency of the device.

T_{SiN}	TE Mode Plot	Mode confinement factor in LN
200 nm	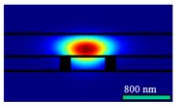	76.8%
80 nm	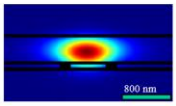	86.0%
40 nm	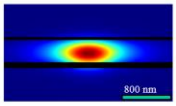	89.7%

Figure 5.3: Three different simulations of wafer-bonded hybrid SiN/LN waveguide. Thickness of LN layer is 300 nm; width of SiN ridge is 800 nm; thickness of SiN ridge is varied.

Additionally, the structure shown in Figure 5.1(b) can act as a waveguide, with only a SiN ridge on a quartz handle, prior to wafer-bonding. Therefore, this structure was also simulated and a TE mode was found. Several iterations of fabrication were performed, where the SiN was patterned by electron beam lithography (EBL) and inductively coupled plasma (ICP) etching, and the step height was measured in an atomic

force microscope (AFM). On one iteration, the step height was 187 nm, and from this, it became clear that the SiN was under-etched in this process. With this in mind, the under-etched waveguide was simulated with step heights of 180 nm and 190 nm, and it was found that the waveguide still supported a single TE mode. These results are shown in Figure 5.4.

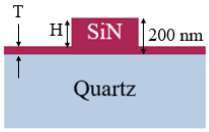

Ridge height, H	200 nm	190 nm	180 nm
Slab Thickness, T	0	10 nm	20 nm
Number of modes	1	1	1
Mode Plot	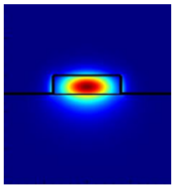	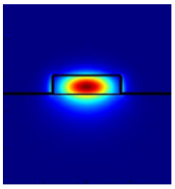	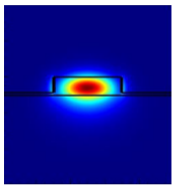

Figure 5.4: Simulations of SiN on Qz waveguide; second and third columns show simulations of under-etching.

On another iteration of the fabrication process, after etching the SiN, the step height was measured to be 295 nm. This indicated that the sample was over-etched; the gas recipe used in the ICP etched the quartz as well as the nitride. After this, the waveguide was simulated again in an over-etched state, and it was found that it still supported a TE mode. These results are shown in Figure 5.5.

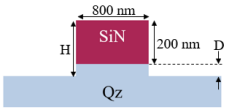

	Simulation #1	Simulation #2
D (etch depth in quartz)	95 nm	100 nm
H (overall ridge height)	295 nm	300 nm
Mode Plot	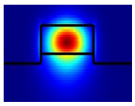	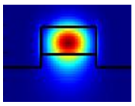

Figure 5.5: Simulations of SiN on Qz waveguide, showing over-etching.

Ultimately, after this iteration of the fabrication process, light was coupled into the waveguides using a 1064 nm laser, and it was found that the overall loss in the waveguide was 34.2 dB, for a 10 mm long straight waveguide, which includes coupling loss as well as propagation loss through the waveguide. A PECVD SiO_2 cladding was deposited on this sample, but this did not significantly change the result. To the best of our knowledge, SiN waveguides have never appeared before in published literature at 1064 nm but, for comparison, loss of 0.62 dB/cm was achieved in a similar waveguide at the 900 nm wavelength [21].

Wafer-bonding with adhesive materials was also explored in simulations. Instead of direct wafer-bonding, benzocyclobutene (BCB) can be used as an adhesive between the two wafers. BCB is available under the trade name Cyclotene 3022-35, from Dow Chemical Company. After forming the SiN waveguides, it is possible to spin-coat the wafer with BCB and then bond the lithium niobate wafer on top (Figure 5.6(a)).

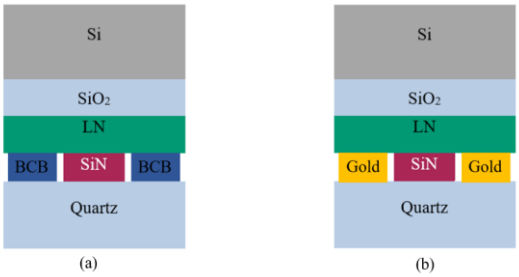

Figure 5.6: Wafer-bonding with adhesive materials. (a) Wafer-bonding with BCB. (b) Wafer-bonding with gold.

When using BCB, handle removal is also necessary, in a manner similar to the direct wafer-bonded structure. During the bonding process, it is possible that the TFLN ends up in contact with the SiN, or it is possible that the layer of BCB is thicker than the 200 nm SiN ridge, and, thus, a thin layer of BCB ends up between the two materials.For this reason, simulations were run with varying amounts of BCB. Figure 5.7 shows one of these results, in which a 300 nm thick layer of BCB still results in a single guided mode. Through a series of simulations, it was found that the BCB could be up to 400 nm thick, and still allow for a single mode shared between the silicon nitride, BCB, and lithium niobate.

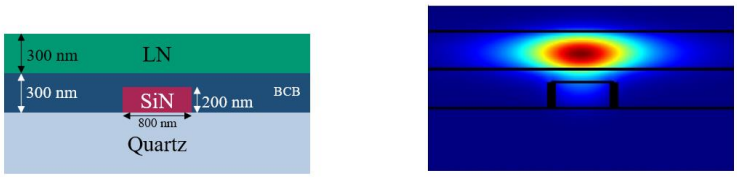

Figure 5.7: Optical simulation of waveguide, at 1064 nm, with 300 nm thick layer of BCB.

Another possibility is to perform wafer-bonding with gold on both wafers (Figure 5.6(b)). This offers an advantage, which is that the gold serves dual duty, as the bonding

material and as the electrodes of the modulator. Therefore, handle removal is not necessary. The waveguide was simulated with this configuration. Not surprisingly, it was found that the structure supports a single TE optical mode. In this case, optical loss is an issue, due to metal absorption, resulting from the gold being in close proximity to the SiN waveguide. A simulation was run where the distance between adjacent gold pads was 6 μm, and it was found that the material absorption loss is 0.0017 dB/cm. In practice, this loss will be higher due to sidewall roughness of the SiN. A plot of the resulting mode for a 6 μm gap is shown in Figure 5.8(a). A sweep was performed over gap values ranging from 3 μm to 6 μm, and this is shown in Figure 5.8(b).

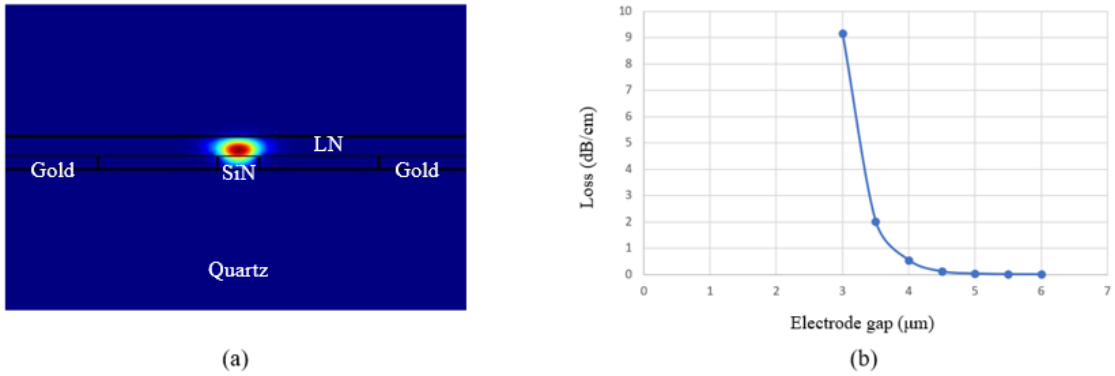

Figure 5.8: Simulations of wafer-bonded LN/SiN waveguide with gold. (a) TE mode plot with 6 μm gap. (b) Plot of optical loss versus electrode gap.

A three-dimensional visualization of this process is shown in Figure 5.9. After forming the SiN ridges, gold must be deposited in a specific pattern around the ridges. Then, the LN wafer must be diced to a smaller size than the first wafer, and more gold must be deposited on this second wafer, in a matching pattern. The LN wafer is then inverted and bonded to the SiN wafer, and because of its smaller size, some gold is left

exposed to serve as the electrodes. These electrodes can be probed using tungsten probe tips as described in Chapter 2. This process has the advantage that handle removal is not required.

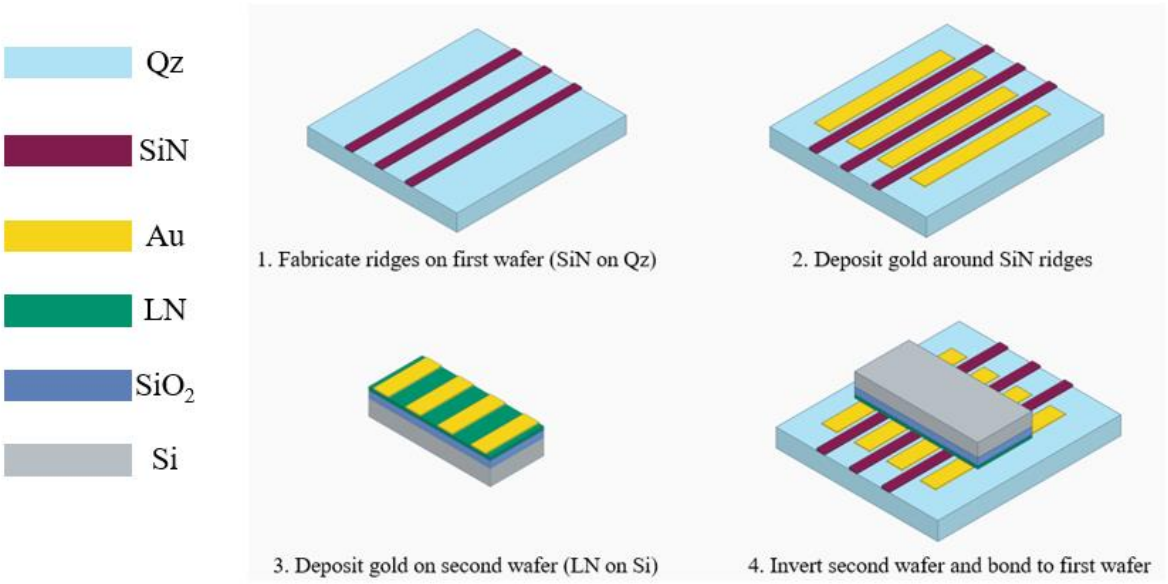

Figure 5.9: Three-dimensional visualization of wafer-bonding procedure with gold**.**

Chapter 6

LOW-FREQUENCY PHASE MODULATOR IN TFLN AT 1064 NM

As an alternative to wafer-bonding, a phase modulator based on an etched LN ridge waveguide was considered. This turned out to be successful, and a device was simulated, fabricated and characterized that is capable of guiding and modulating light at the 1064 nm wavelength. A schematic of the device is shown in Figure 6.1. Two coplanar gold electrodes are present around the waveguide to apply the modulating voltage signal. The electrodes of the device are 100 nm thick, which allows modulation of the light, but does not enable high-frequency operation. Thus, the device was tested at a low frequency, 1 kHz.

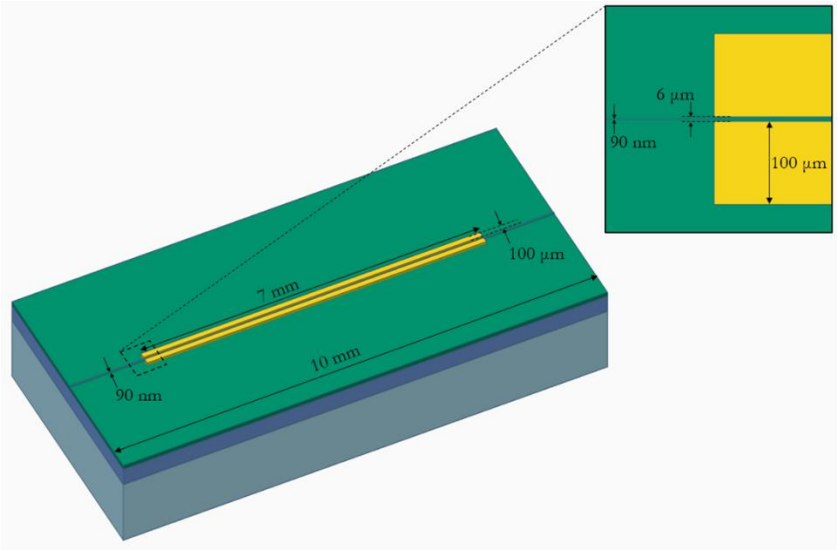

Figure 6.1: Schematic of $LiNbO_3$ phase modulator with etched LN ridge waveguide.

6.1 Simulation

Simulations were run based on wafers available from NanoLN, which contain a 600 nm thick X-cut LN layer, attached to a 500 μm thick quartz handle. Between the LN layer and the handle is a 2.7 μm thick bonding layer of PECVD SiO_2. The wave-guiding portion of the device was simulated in Lumerical MODE Solutions software. Simulations were run, varying the ridge width and the etch depth. The chosen structure includes a ridge with a top width of 900 nm and an etch depth of 90 nm.

A cross-section of the device, including the ridge waveguide and the electrodes, is shown in Figure 6.2. Simulation of this structure, with a 6.0 μm gap, resulted in a TE mode and a TM mode, with effective refractive indices of 2.0308 and 2.0629. The simulation gives 0.68 dB/cm for the material absorption loss of the TE mode, and its mode plot (inset in Figure 6.2) shows a non-negligible leakage of light into the buried oxide layer, which is the likely reason for this loss. Surface roughness was not included in the simulation.

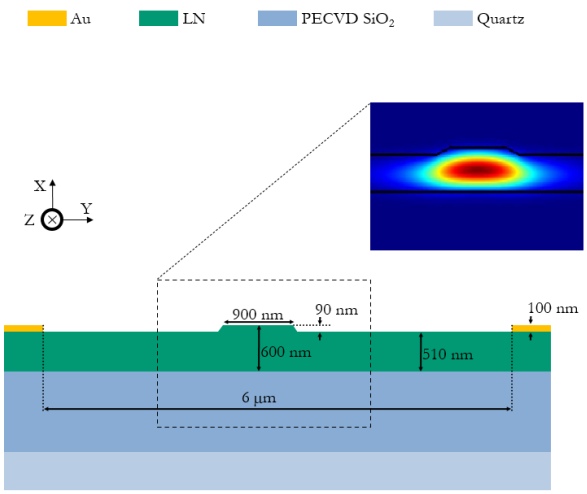

Figure 6.2: Cross-section diagram of $LiNbO_3$ phase modulator. Inset shows mode plot of the TE optical mode, resulting from the simulation in Lumerical MODE Solutions.

Additional simulations were run in which the gap between the gold electrodes was varied, with the electrodes located symmetrically around the ridge in all cases. There is a trade-off; a smaller gap has the advantage of reducing V_π, but it also has the disadvantage of increasing optical absorption loss due to the optical mode interacting with the metal. A portion of these simulation results are shown in Figure 6.3; a 6.0 µm gap resulted in one TE mode with a loss 0.68 dB/cm, which is acceptable. The same simulation with a 4.0 µm gap resulted in two TE modes, which is undesirable; these two modes had loss values of 1.40 dB/cm and 25.61 dB/cm. Because of these simulations, it was decided that 6.0 µm would be the minimum gap size.

	Simulation #1	Simulation #2	
G (gap between electrodes)	6.0 μm	4.0 μm	
Total number of TE modes found	1	2	
Mode Plots	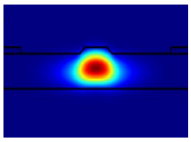 TE polarization fraction: 77% Loss: 0.68 dB/cm	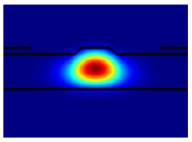 TE polarization fraction: 91% Loss: 1.40 dB/cm	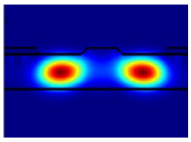 TE polarization fraction: 71% Loss: 25.61 dB/cm

Figure 6.3: Simulations of LN ridge waveguide, at 1064 nm, varying the size of the electrode gap. © 2021 IEEE

6.2 Fabrication

The fabrication steps of the device are illustrated in Figure 6.4. First, the 3-inch round wafer was diced into 16 mm × 18 mm rectangles. On one of these rectangular pieces, an 80 nm layer of chromium (Cr) was deposited by physical vapor deposition (sputtering). Then the Cr surface was cleaned and prepared with AR 300-80 adhesion promoter, and a layer of AR 7520.18 resist was spin-coated on top of the Cr. The resist was patterned by electron beam lithography (EBL), to define 900 nm wide lines. This line pattern was transferred into the Cr layer by inductively coupled plasma (ICP) etching, with a gas recipe consisting of chlorine (Cl_2) and oxygen (O_2), at an etch rate of 1.3 nm/sec. After this, all remaining resist was removed by O_2 ashing in a plasma cleaner, leaving only the patterned chromium. The pattern was then transferred from the Cr into the LN layer by a second stage of ICP etching, using tetrafluoromethane (CF_4) and argon (Ar), with an etch rate of 0.3 nm/sec. This etch is anisotropic and directional, and it was time-multiplexed to ensure that the LN was not damaged by thermal stress. This time-multiplexing consists of a one-minute cycle of etching with 600 W plasma and 400 W

bias, and a 1.5-minute cycle of cooldown with 0 W bias. Once the LN etching was complete, the remaining Cr was removed by wet etching in ceric ammonium nitrate, completing the formation of the waveguides. Each waveguide is 10 mm in length.

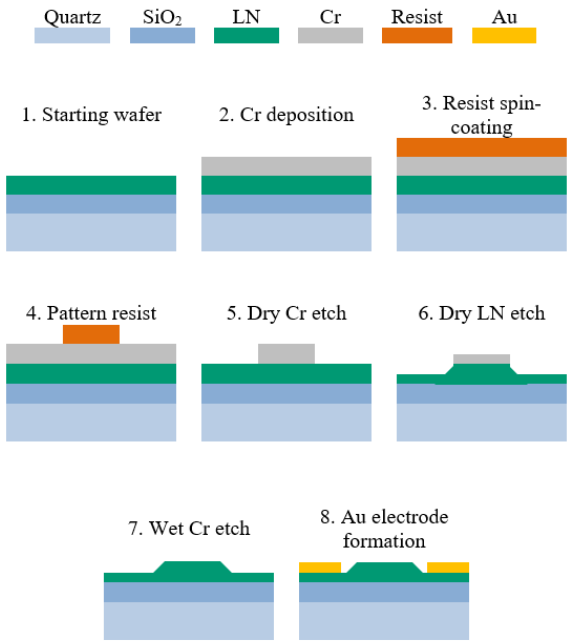

Figure 6.4: Fabrication schematic of low-frequency phase modulator. © 2021 IEEE

Next, to form electrodes, a bi-layer of photoresist was spin-coated and patterned through laser lithography. Metal was deposited onto the sample using electron beam physical vapor deposition (EBPVD), including a 4 nm thick titanium adhesion layer, followed by a 100 nm thick layer of gold. After deposition was complete, liftoff was performed by submerging the sample in acetone in an ultrasonic cleaning bath for five minutes. The electrodes have a length of 7 mm, and each waveguide has two electrodes around it, with a gap of 6 µm. After electrode formation, the sample was diced to expose

the end facets of the waveguides, and these facets were polished at a 15-degree angle, using a series of diamond lapping films.

6.3 Characterization

Two variations of this device were fabricated and characterized. In the first variation, the electrode gap was chosen to be 10 μm, to provide easier fabrication tolerances. The $V_{\pi,45^\circ}$ of this device was measured, as described in Chapter 2, and it was found to be 9.4 V. Substituting into equation 2.10 gives a measured value of $V_{\pi,TE}$ = 6.16 V. Since the electrodes are 7 mm long, this results in a value of 4.31 V-cm for the device's modulation efficiency per unit length ($V_\pi L$).

The second variation of the device included a 6 μm gap, and the $V_{\pi,45^\circ}$ was measured to be 4.2 V. Substituting into equation 2.10 gives a measured value of $V_{\pi,TE}$ = 2.75 V and a value of 1.91 V-cm for the device's $V_\pi L$. The voltage signals resulting from this characterization are shown in Figure 6.5.

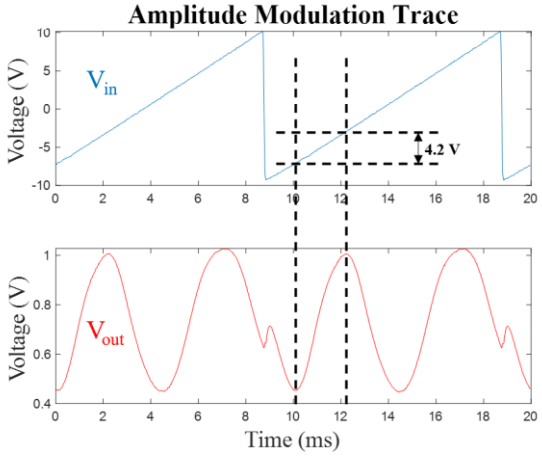

Figure 6.5: Voltage signals resulting from electro-optic modulator characterization.

In addition to this V_π measurement, optical power measurements revealed that the overall insertion loss was 20 dB, which is due to fiber-to-chip coupling loss as well as on-chip propagation loss in the waveguide. The propagation loss was measured to be 7.7 dB/cm by preparing separate samples and performing a cutback measurement. This is significantly higher than the simulated value, which makes sense because the fabricated device has sidewall roughness which was not accounted for in the simulation. Other ICP etched thin-film $LiNbO_3$ ridge waveguides appear in the literature with similar propagation loss [26], [34]; however, it is worth noting that researchers have achieved propagation losses of 0.4 dB/cm using more meticulous fabrication techniques [35].

Since the device is 1 cm long, 7.7 dB of loss results from optical propagation through the waveguide, and approximately 6.15 dB of loss results from coupling loss at the entrance facet and exit facet. This coupling loss is due to poor mode matching between the lensed fibers and the waveguide facet. The lensed fibers have a spot size of 2.5 μm, and the LN waveguide has a mode diameter of ~4.5 μm. Coupling loss could be improved in future work by implementing a taper structure, grating couplers, or a high-numerical-aperture fiber at the input and output.

Chapter 7

HIGH-FREQUENCY PHASE MODULATOR IN TFLN AT 1064 NM

Another device was investigated: a hybrid SiN/LN electro-optic phase modulator that uses a wavelength of 1064 nm. It uses the rib-loaded waveguide design discussed in Chapter 3. It is expected to operate at frequencies from 0 to 50 GHz, thus covering a portion of the mmW spectrum. For this device, it was necessary to perform additional fabrication procedures, including electroplating, to form electrodes capable of high-frequency operation.

7.1 Simulation

7.1.1 Simulations in Lumerical MODE Solutions

The waveguide consists of a 300 nm thin-film LN layer, with a SiN ridge. The ridge has a width of 800 nm and a thickness of 200 nm. Simulation of this structure resulted in one guided optical mode with an effective optical group index of 1.9397 and a loss of 0.0026 dB/cm, as shown in Figure 7.1.

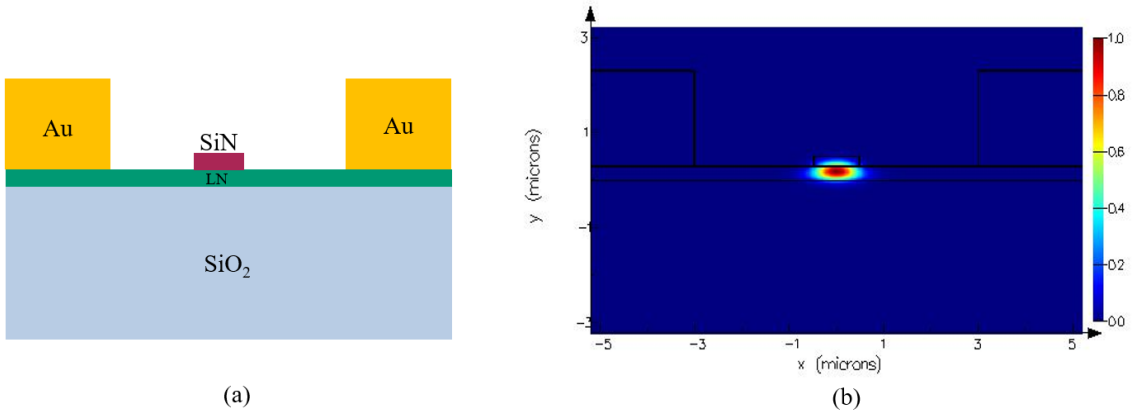

Figure 7.1: Hybrid SiN/TFLN modulator. (a) Cross-section of modulator. (b) TE mode plot resulting from simulation.

Additionally, the structure was simulated repeatedly, varying the size of the electrode gap. This is shown in Figure 7.2; as expected, smaller electrode gaps result in greater optical loss. When the gap size was reduced to 2 μm, the result was that no TE modes were found. Based on these simulations, a 6 μm gap was chosen for the fabricated device.

Gap (μm)	Loss of TE mode (dB/cm)
2	No TE mode found
2.5	41.628
3	10.935
3.5	2.5839
4	0.70831
4.5	0.15839
5	0.043309
5.5	0.0098175
6	0.0025663

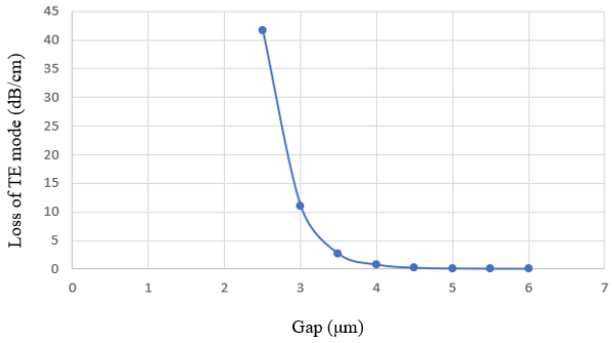

Figure 7.2: Simulation of optical loss versus electrode gap for hybrid SiN/LN device.

7.1.2 Simulations in Ansys HFSS Electronics Desktop

In Ansys HFSS, the three-dimensional structure of the modulator was created, including GSG CPW electrodes and optical waveguides. Gold, silicon, and silicon nitride

are modeled using default material properties. The LN is modeled as a custom anisotropic material, with two values of permittivity, ε_e = 28 and ε_o = 44. The electrode structure (Figure 7.2(a)) includes a probe region, a taper region, and an interaction region. The probe region consists of three rectangles; the first is 211 μm × 200 μm; the second and third are 100 μm × 200 μm. The thickness of the electrodes is 2 μm. The spacing in the *y*-direction between these rectangles is 32 μm. The probe region was simulated, and it was found that the characteristic impedance ranges from 56 ohms to 57 ohms over the frequency range from 0 to 100 GHz, as shown in Figure 7.2(b). This is an acceptable match for 50 ohm impedance of the GSG probes.

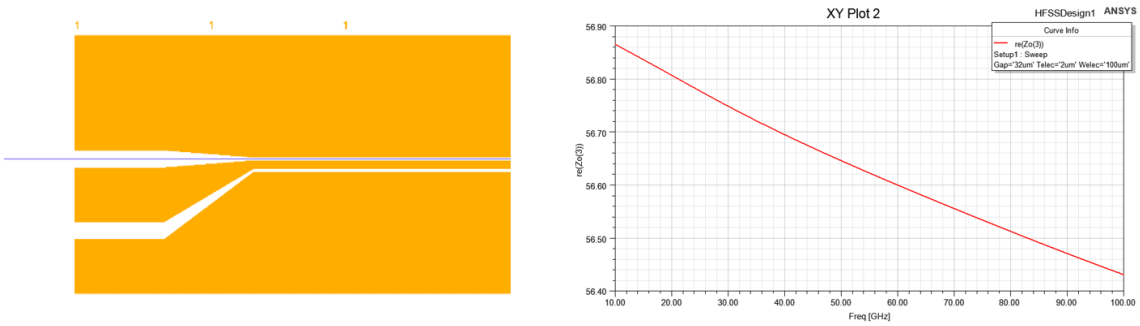

(a) (b)

Figure 7.3: (a) Diagram of GSG CPW electrodes. (b) Plot of characteristic impedance vs frequency for the probe region of the electrodes.

The interaction region is again made up of three rectangles; the first and third rectangles are ground electrodes and they both have dimensions of 222 μm × 16 mm. The second rectangle is the signal electrode, and it is 15 μm × 16 mm. The gap between the rectangles is 6 μm. Following the theory of GSG CPW electrodes, only the signal width of 15 μm and the gap width of 6 μm are relevant. The taper region consists of trapezoids,

allowing the electrodes to taper from the probe region to the interaction region over a 200 μm length.

For the interaction region of the GSG CPW, the n_{RF} was found in the simulation as the square root of the dielectric constant, epsilon. A plot of this is shown in Figure 7.3, where it is found that the n_{RF} ranges from 2.02 to 2.07 over the frequency range from 10 GHz to 100 GHz.

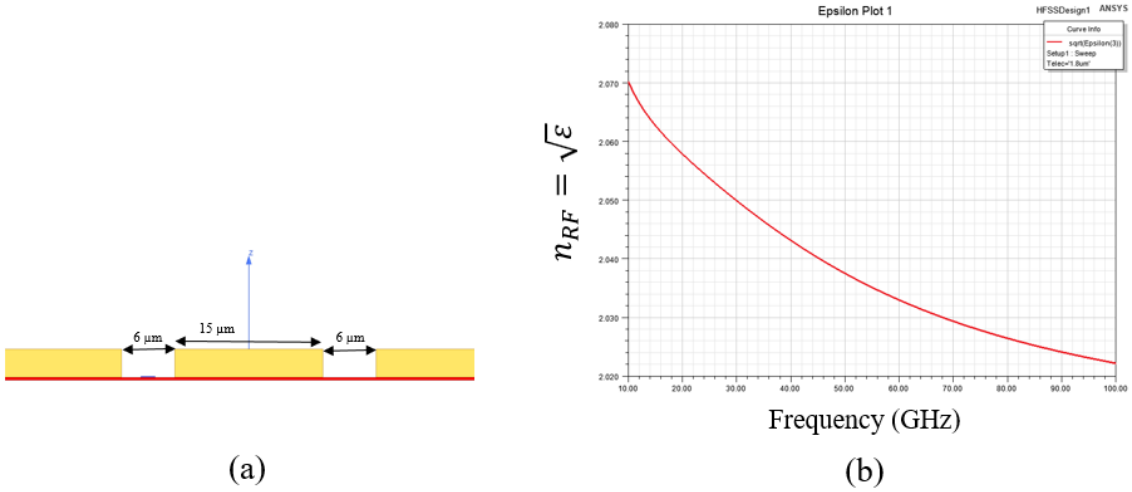

Figure 7.4: (a) Cross-section of GSG CPW electrodes. (b) Simulated results of n_{RF} as a function of frequency.

For efficient high-frequency operation, it is essential to match the group index of the optical mode (n_g) to the phase index of the RF mode (n_{RF}), such that the two modes co-propagate through the modulator; this is known as index matching or velocity matching. Therefore, n_g was calculated by running multiple optical simulations in Lumerical and using the following formula:

$$n_g = n - \lambda_0 \frac{dn}{d\lambda_0}. \tag{7.1}$$

The derivative, $dn/d\lambda_0$ was approximated by running three simulations at three different wavelengths, 1014 nm, 1064 nm, and 1114 nm, and finding the slope of the line between the three points. This resulted in a value of $n_g = 2.214$ for the group index. Comparing this with the simulated n_{RF}, it is clear that n_{RF} must be increased for this device, which corresponds to increasing the velocity of the applied modulating voltage signal. This can be achieved by introducing a buffer layer with a low dielectric constant, such as cladding the waveguide with UV15.

Additionally, the RF electric field was simulated and plotted in Ansys HFSS; this plot is shown in Figure 7.4. In the simulation, the voltage applied to the electrodes is 1 volt. This resulted in an electric field which was highest in the region near the gold electrodes, with an approximate value of 2.07×10^6 V/m.

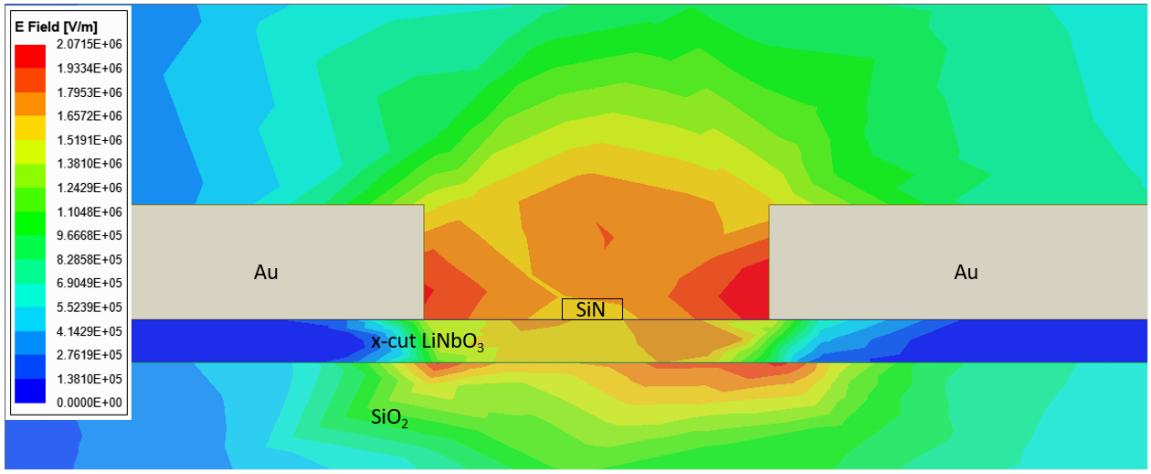

Figure 7.5: Simulated RF electric field distribution for hybrid SiN/LN device. In the simulation, 1 V is applied from signal to ground.

7.2 Fabrication

The fabrication steps for this device are illustrated in Figure 7.5. The starting wafer was purchased from NanoLN and includes four layers, as shown in Figure 7.5(a): a

500 µm thick Si handle, a 4.7 µm bonding layer of PECVD SiO_2, a 300 nm thin-film LN layer, and a 200 nm layer of LPCVD SiN. This wafer was diced into 22.5 mm × 22.5 mm square samples. Fabrication on each sample began with electron beam lithography, and thus the initial fabrication steps were similar to the low-frequency device described in the previous chapter: Cr deposition, resist spin-coating, resist patterning, followed by Cr dry etching in an ICP. The next step was dry etching of the SiN layer, in the ICP, using sulfur hexafluoride (SF_6), octafluorocyclobutane (C_4F_8), and argon (Ar), at an etch rate of 2.5 nm/sec. Next, the remaining Cr was removed with a wet etch in ceric ammonium nitrate, completing the formation of the hybrid waveguides. Each waveguide is 20 mm in length.

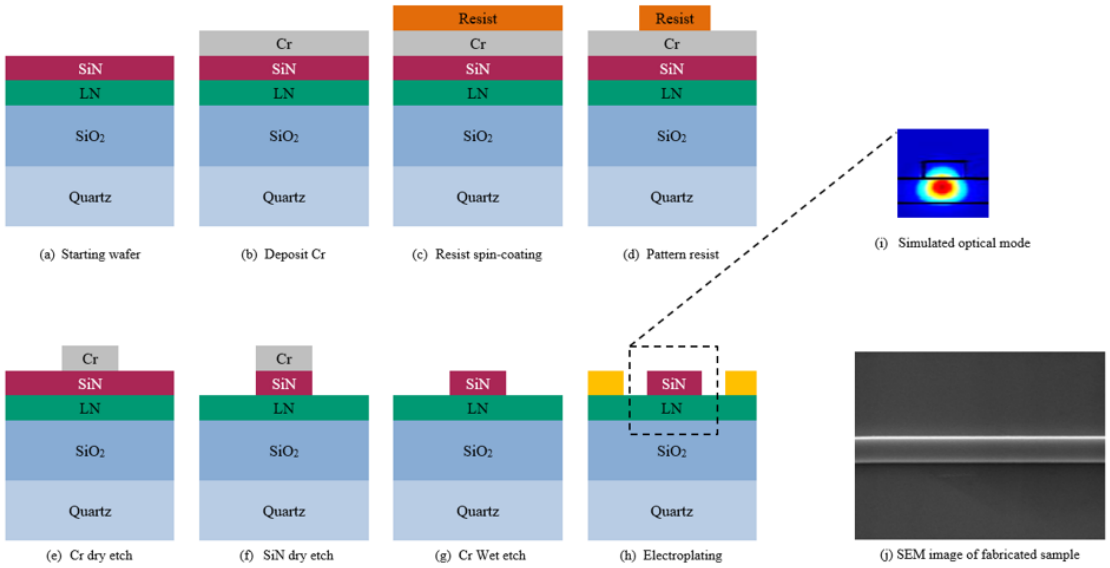

Figure 7.6: Fabrication schematic of high-frequency hybrid SiN/TFLN modulator.

After this, electrodes were formed around the waveguides. The electrode formation is significantly different than electrode formation for the low-frequency modulator; electroplating is used instead of liftoff, to achieve a 2 µm thickness. This

fabrication process is shown in Figure 7.6. First, a Ti/Au/Ti seed layer was deposited, with 10 nm of Ti, 50 nm of Au, and 10 nm of Ti. This was followed by spin-coating with AZ P4330 photoresist. Next, the photoresist was exposed in a Heidelberg MLA100 Laser writer, with a dose of 700 mJ/cm^2, using appropriate alignment marks to ensure that the waveguides were parallel to the electrodes and centered in the gap. The photoresist was developed, and then a wet etch was performed by submerging the sample for 40 seconds in a HF:H_2O_2:H_2O solution, to remove the top layer of Ti within the seed layer. The sample was electroplated in a bath of Elevate Gold 7990 solution for 2.5 hours, with 0.6 mA current. Electroplating was followed by photoresist removal with a mixture of H_2SO_4 and H_2O_2 (piranha solution), and then seed layer removal with a wet gold etch containing potassium iodide. Once this was complete, the end facets of the waveguides were diced to expose the waveguide end facets and polished with a series of diamond lapping films.

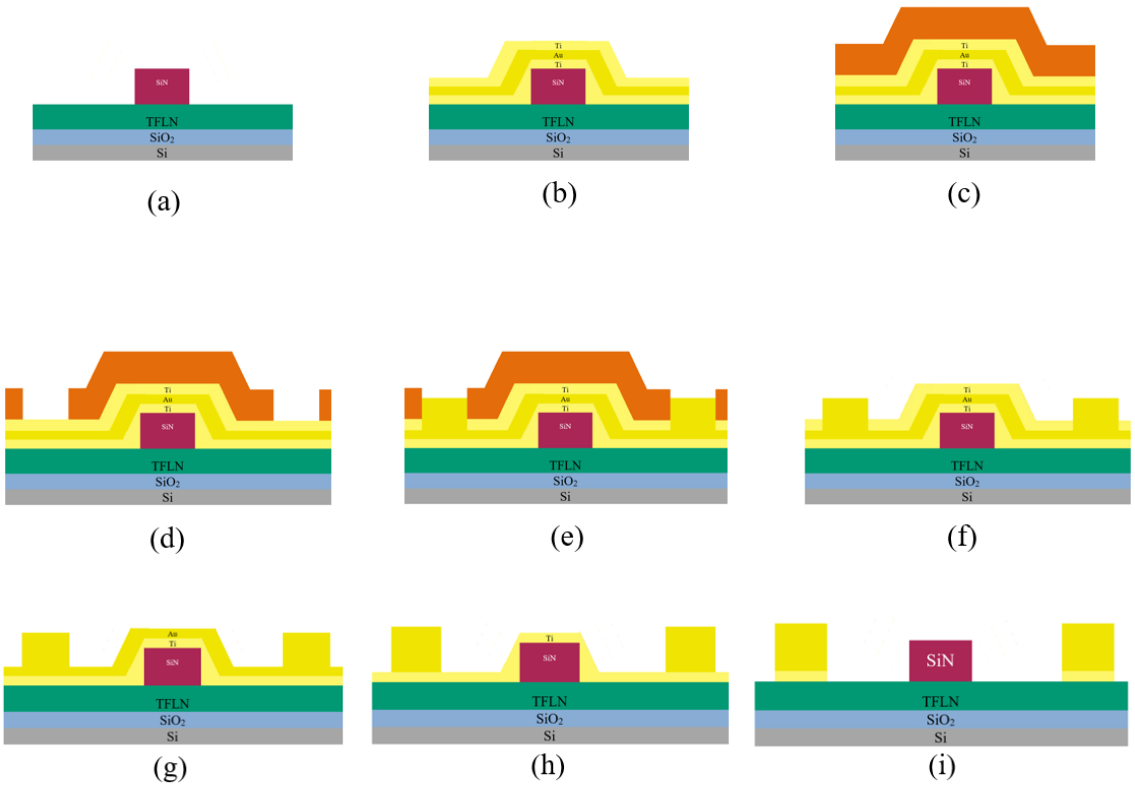

Figure 7.7: Electrode fabrication procedure. (a) Hybrid SiN/TFLN ridge waveguide. (b) Deposition of Ti/Au/Ti seed layer. (c) Photoresist spin-coating. (d) Sample after exposure and developing. (e) Electrodes are built up by electroplating. (f) Photoresist removal. (g) Removal of top Ti layer. (h) Removal of Au layer. (i) Removal of bottom Ti layer.

7.3 Characterization

The electrodes of the device were characterized using an Agilent E8316C Programmable Network Analyzer (PNA), as described in Chapter 2. Two GSG probes with 100 μm pitch, fed by 1 mm cables, were touched down on the sample, one on either side of the electrode. The PNA measures S_{12} and S_{21} by applying an appropriate voltage through one probe, and measuring the transmission received by the other probe. Similarly, S_{11} and S_{22} are found by measuring reflection from a probe onto itself. A sweep

was performed from DC to 50 GHz; the resulting S-parameters as a function of frequency are shown in Figure 7.7.

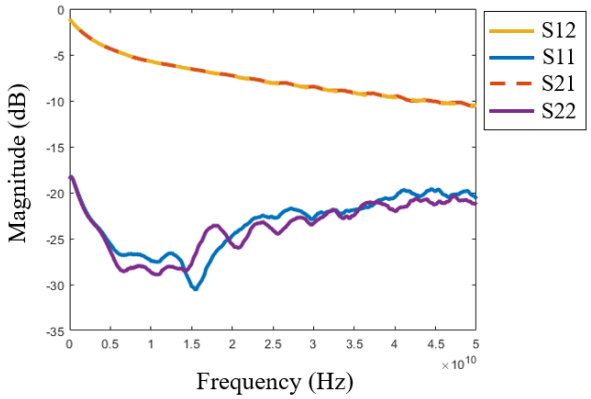

Figure 7.8: Measured S-parameters of electrodes in high-frequency modulator.

Additionally, it is possible to calculate loss (α) as a function of frequency, based on S_{11} and S_{21}, according to the following formula, presented in a 2008 publication by Wu [22]:

$$\alpha = -\frac{1}{l} \cdot ln\sqrt{(|S_{11}|^2 + |S_{21}|^2)} \quad (Np/m).$$

This was done by exporting the S-parameter data from the PNA as a CSV file, then importing the CSV file into MATLAB, and implementing this equation as MATLAB code. The value of l, the length of the electrodes, was 1.68 cm. The equation gives α in Nepers per meter, and these values were converted to dB/cm. The resulting plot is shown in Figure 7.8; loss increases with frequency as expected, and ranges from 0.6024 dB/cm to 6.0651 dB/cm.

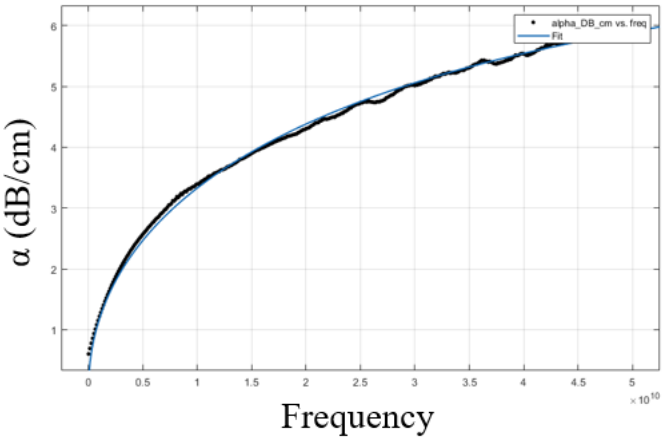

Figure 7.9: Overall loss of GSG CPW electrodes as a function of frequency, with curve fit.

Chapter 8

DESIGN OF INTENSITY MODULATOR IN TFLN AT 1064 NM

To produce an electro-optic intensity modulator, the optical signal must be split into two paths and then re-combined, forming an MZM, as described in Chapter 2. The standard technique for this is to use multimode interference (MMI) coupler, with a 1×2 MMI as the splitter and a 2×1 MMI as the combiner. It is not possible to produce a perfect 50-50 split, so extensive simulation work was done to design these MMIs and get as close as possible to 50-50.

Figure 8.1: Schematic of intensity modulator.

The three-dimensional structure of a 1×2 MMI was constructed in Lumerical, and the available computational solvers were used to compute the optical properties of the structure. The Finite Difference Eigenmode (FDE) solver simulates cross-sections of the device. After running multiple FDE simulations with varying widths, a value of 1.3 µm was chosen for the core width of the MMI. This resulted in four modes, as shown in Figure 8.2, with a pattern that is desirable for 1×2 MMI operation. Of these four modes, one is a TE mode with a central maximum, which matches with the input waveguide.

One of them is a TE mode with two central maxima, matching with the two output waveguides. After selecting the core width to be 1.3 µm, the width of the input waveguide was chosen to be 0.5 µm, which is less than half of 1.3 µm and results in one mode in the FDE solver.

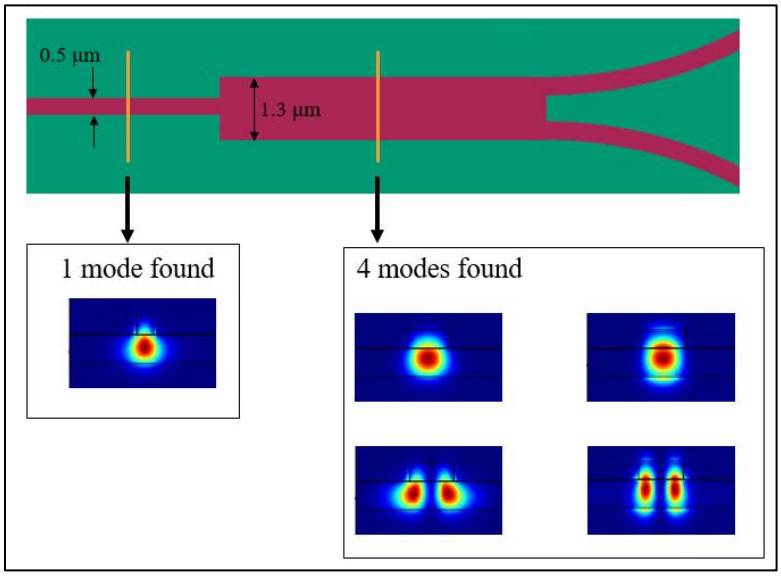

Figure 8.2: Results of simulation of cross-sections of MMI. In the region of 0.5 µm width, one mode was found. In the region of 1.3 µm width, four modes were found. This is desirable for 1×2 MMI operation.

The Eigen Mode Expansion (EME) solver was also used, as it is the more rigorous and more reliable solver for MMIs. An EME simulation was set up with three ports, one port on the input waveguide and one port on each output waveguide. The results of this simulation give a 3×3 S-matrix. The initial simulation, including curved waveguides at the outputs, gave a value of 0.34 for $|S_{21}|^2$ and $|S_{31}|^2$, which are the fractions of optical power appearing at the two output waveguides. This gives a sum of 0.68, or 68%. Ideally this sum would be 100%, indicating that 100% of the optical power

at the input appears at the output. However, in all EME simulations, this value always ends up being less than 100% due to simulation errors.

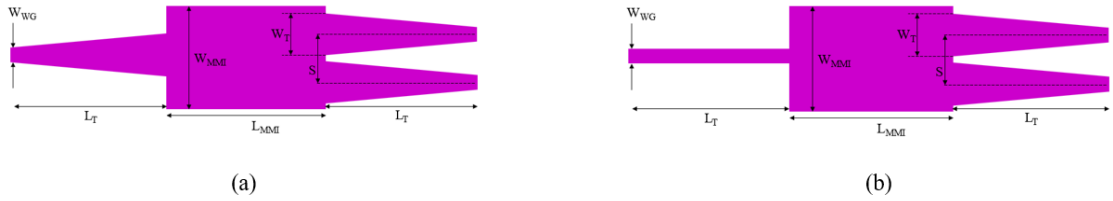

Figure 8.3: Diagram of multi-mode interference (MMI) coupler. (a) MMI with tapered input and two tapered outputs. (b) MMI with non-tapered input and two tapered outputs.

Subsequently, an MMI with straight tapered waveguides was simulated, in two variations. The first variation has a tapered input and two tapered outputs, Figure 8.3a. The second variation has a non-tapered input, as shown in Figure 8.3b. In both cases, there are six dimensions that can be varied, as shown in the diagrams: the width of the waveguide (W_{WG}), the width of the MMI (W_{MMI}), the length of the MMI (L_{MMI}), the taper width (W_T), the spacing between the waveguides (S), and the length of the taper (L_T). Whenever the EME solver is used, the structure must be divided into multiple cells, labeled as “group spans” within the simulation software. For these simulations, there were three group spans, dividing up the structure along the z axis, which is the direction of light propagation. The first group span had a length of L_T, the second had a length of L_{MMI}, and the third had a length of L_T. Whenever these lengths were modified for a new simulation, the lengths of the EME group spans were also manually updated to match up with the new values of L_T and L_{MMI}. Furthermore, the first and third group spans were divided into 10 subcells each, which was necessary because these are the group spans that

contain the tapers, with varying cross-section, which required more subcells for a more accurate result. The first and third group spans also included mesh override regions, which divided up the structure into a finer mesh (0.02 μm mesh step) and also increased the accuracy of the result.

It was found that the layout in Figure 8.2a, with an input taper, produced better results than the layout in Figure 8.2b. The results were assessed by looking at the 3×3 S-matrix produced by the simulation, especially $|S_{21}|^2$. In the ideal case, $|S_{21}|^2 = 0.5$, which would mean that 50% power appears at the output and the MMI is behaving as an ideal 50:50 beam splitter. However, in the real simulations, $|S_{21}|^2$ is always less than 0.5 due to optical loss and simulation errors. Selected results from simulations are shown in Table 8.1, indicating the best values found. For the structure in Figure 8.2a, with a tapered input, the highest value of $|S_{21}|^2$ was 0.47283, with dimensions given in the first row of Table 8.1. Meanwhile, for the MMI with the non-tapered input, the highest value of $|S_{21}|^2$ was 0.457678, with the dimensions given in the second row of Table 1.

MMI Layout	**W_{WG}**	**W_{MMI}**	**L_{MMI}**	**W_T**	**S**	**L_T**	**$\|S_{21}\|^2$**
Tapered input (Figure 8.2a)	0.8 μm	3.1 μm	8.5 μm	1.3 μm	1.6 μm	10 μm	0.47283
Non-tapered input (Figure 8.2b)	0.8 μm	3.0 μm	8.5 μm	1.3 μm	1.6 μm	10 μm	0.457678

Table 8.1: Results of simulations of 1×2 MMI, showing the best results for the tapered input and the non-tapered input.

The value of L_{MMI} = 8.5 μm was chosen by visualizing the field profile in the simulation software and choosing a value such that the light propagates in a mode with

two maxima, at the location of the two output waveguides. Additionally, a sweep was performed, over values of L_{MMI} ranging from 7.9 µm to 8.6 µm. Similarly, sweeps were performed for all six values, and the value of $|S_{21}|^2$ was checked repeatedly, with 0.47283 as the highest value found. This means that if the MMI was fabricated, 47.283% of the optical power would end up in the first output waveguide and 47.283% would end up in the second output waveguide, which is acceptable for an intensity modulator.

Chapter 9

POTENTIAL FOR SYSTEM INTEGRATION

9.1 Analog Photonic Link System at 1064 nm

The high-frequency intensity modulator discussed in Chapter 8, if fabricated and packaged, could be used as part of an analog photonic link system, as shown in Figure 9.1, below. A 1064 nm laser is the optical source, and a Programmable Signal Generator (PSG) is used to transmit digital information by means of four-point Quadrature Amplitude Modulation (4-QAM). This electrical signal would be applied as input to the intensity modulator, thus imposing the 4QAM signal onto the optical carrier. A modified uni-traveling carrier photodetector (MUTC PD) receives the modulated light; this device was successfully tested at 1064 nm up to 80 GHz by a member of the research group. This forms an intensity-modulation-direct-detection (IMDD) link.

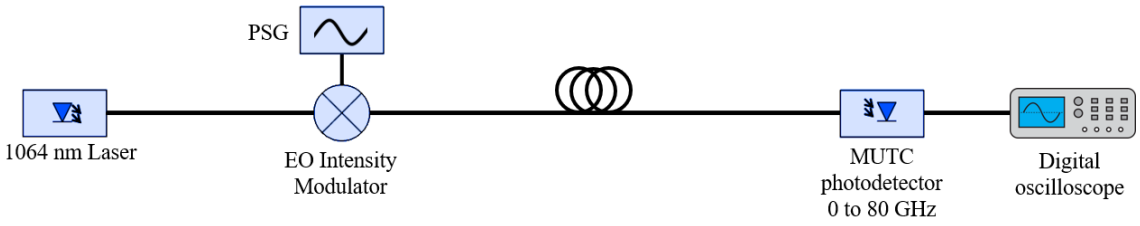

Figure 9.1: Schematic of analog photonic link system.

The electrical output of the PD would be fed into a digital oscilloscope, which will be able to recover the information produced by the PSG in the form of a constellation diagram. Initial tests would be performed from 0 to 2 GHz, which is the default limitation

of the PSG and the oscilloscope. However, this system could be extended to higher frequencies by using range extender devices. In theory, this entire system will be able to perform from 0 to 80 GHz, because 80 GHz is the 3 dB cutoff frequency of the MUTC PD.

9.2 Single-pixel mmW Antenna system at 1064 nm

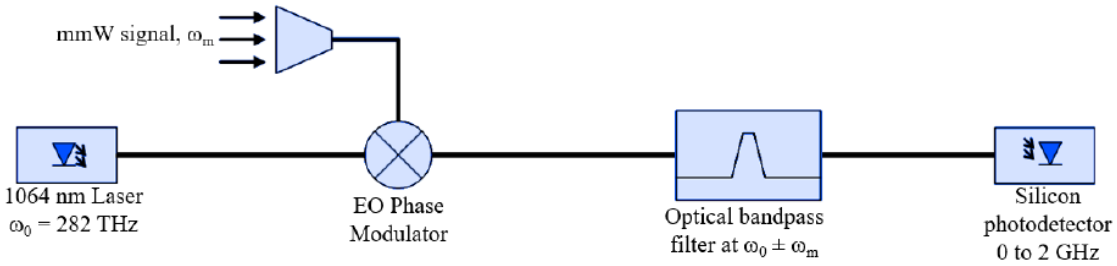

Figure 9.2: Schematic of single-pixel mmW Antenna system.

It is envisioned that the high-frequency EO phase modulator, described in Chapter 7, will be incorporated into a system that can image and detect millimeter waves. After the modulator is fabricated and packaged, it can be set up in the configuration shown in Figure 9.2. In this system, mmW signals in the range of 30 GHz to 100 GHz are received by an antenna and applied as electrical input to the modulator. The modulator up-converts the signals, using the 1064 nm laser as an optical source, such that the light exiting the modulator consists of two sidebands on an optical carrier (Figure 9.3a). Then, this light passes through an optical bandpass filter, which suppresses the carrier and the upper sideband. After the filter, the lower sideband remains, and its amplitude is detected by a silicon photodetector. It is not necessary for this photodetector to operate at mmW

frequencies, because it is merely detecting the amplitude of the lower optical sideband. Therefore, the photodetector will most likely be a low-cost off-the-shelf device, Si-based, and CMOS-compatible, with an operating frequency from 0 Hz to 2 GHz. A similar system was constructed in 2007, using a wavelength of 1550 nm, and was effectively used for imaging purposes [3]. Even though the photodetector was essentially a single pixel, the 2007 publication reported that image reconstruction techniques were successfully used to reproduce a full mmW scene.

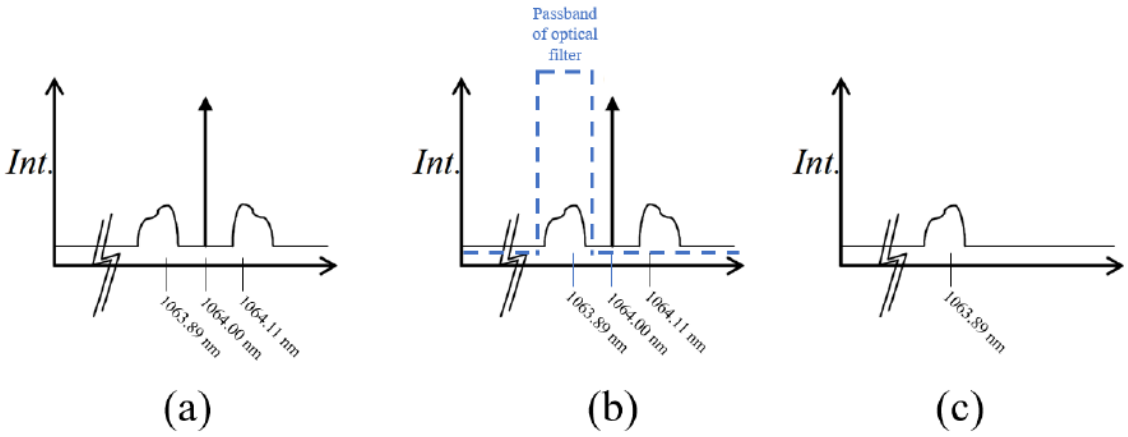

Figure 9.3: Spectra of optical signals in mmW imaging system. (a) Spectrum of optical signal after exiting phase modulator. (b) Dashed line indicates effect of filter. (c) Spectrum of optical signal after the filter.

For the system constructed in 2007, the optical filters were manufactured by the Alluxa corporation. Figure 9.3(b) shows the requirements of the optical filter; it must pass the sideband at 1063.89 nm and block the carrier at 1064 nm. Therefore, the filter must have a transition from high transmission to high blocking within 0.11 nm, which is a very stringent requirement. This requires a state-of-the-art filter and angle-tuning may also be necessary. Furthermore, the sideband will be approximately 20 dB down from the

carrier, which means that the filter must have an optical density of at least OD2 to meet the requirements. This can be achieved by using a stack of multiple filters, if necessary.

Chapter 10

CONCLUSION

It is clear that the combination of TFLN with the 1064 nm wavelength is viable, as demonstrated by the fabricated devices and the simulations presented in this thesis. Mechanically thinned modulators, rib-loaded modulators, wafer-bonded modulators, and dry-etched LN modulators have all been explored at this wavelength. The limitations and challenges arise from the more stringent requirements in the fabrication process, including the intricate details of electron beam lithography and the difficulties of electroplating. A waveguide defect of a given size has a greater detrimental effect at 1064 nm, compared to 1550 nm, because the size of the defect must be compared to the wavelength of the light. These modulators certainly do exhibit a lower V_π compared to their counterparts at 1550 nm, which is a distinct advantage. Meanwhile, the use of the 1064 nm wavelength opens the door towards using low-cost COTS photodetectors and image sensors, resulting in an overall reduction in the cost of assembly of a system. With future progress on these devices, mmW imaging systems could be constructed at a lower cost and with greater electrical-to-optical conversion efficiency than previously existing systems.

REFERENCES

[1] E. L. Wooten, K. M. Kissa, A. Yi-Yan, E. J. Murphy, D. A. Lafaw, P. F. Hallemeier, D. Maack, D. V. Attanasio, D. J. Fritz, and G. J. McBrien, "A review of lithium niobate modulators for fiber-optic communications systems," IEEE J. Sel. Top. Quantum Electron. **6**(1), 69–82 (2000).

[2] K. F. Reim, J. Nunn, V. O. Lorenz, B. J. Sussman, K. C. Lee, N. K. Langford, D. Jaksch, and I. A. Walmsley, "Towards high-speed optical quantum memories," Nat. Photonics **4**, 218 (2010).

[3] C. A. Schuetz, J. Murakowski, G. J. Schneider and D. W. Prather, "Radiometric Millimeter-wave detection via optical upconversion and carrier suppression," IEEE Transactions on Microwave Theory and Techniques, **53**(5), 1732-1738, (2005). doi: 10.1109/TMTT.2005.847106.

[4] J. Macario, P. Yao, S. Shi, A. Zablocki, C. Harrity, R. D. Martin, C. A. Schuetz, and D. W. Prather, "Full spectrum millimeter-wave modulation," Opt. Express 20(21), 23623–23629 (2012).

[5] Q. Cheng, M. Bahadori, M. Glock, S. Rumley, and K. Bergman, "Recent advances in optical technologies for data centers: a review," Optica **5**, 1354 (2018).

[6] Forbes, M.; Gourlay, J.; Desmulliez, M., "Optically interconnected electronic chips: a tutorial and review of the technology", Electronics & Communication Engineering Journal, **13**(5), 221-232 (2001).

[7] Andrew J. Metcalf, Connor D. Fredrick, Ryan C. Terrien, Scott B. Papp, and Scott A. Diddams, "30 GHz electro-optic frequency comb spanning 300 THz in the near infrared and visible," Opt. Lett. **44**(11), 2673-2676 (2019).

[8] Jain, Vk & Kaushal, Hemani & A.Vats, "Free space optical communication: laser sources, modulation schemes and detection techniques." (2013). https://arxiv.org/pdf/1506.04836.pdf.

[9] Y. Cui et al., "Enhanced Spurious-Free Dynamic Range in Intensity-Modulated Analog Photonic Link Using Digital Postprocessing," in IEEE Photonics Journal, vol. 6, no. 2, pp. 1-8, April 2014, Art no. 7900608, doi: 10.1109/JPHOT.2014.2308196.

[10] Ruiqiong Wang, Yongsheng Gao, Wuying Wang, Junchang Zhang, Qinggui Tan, Yangyu Fan, "Suppression of third-order intermodulation distortion in analog photonic link based on an integrated polarization division multiplexing Mach–Zehnder modulator," Optics Communications, Volume 475, 2020, 126253, ISSN 0030-4018, https://doi.org/10.1016/j.optcom.2020.126253.

[11] G. T. Reed, G. Mashanovich, F.Y. Gardes, and D. J. Thomson, "Silicon Optical Modulators," Nat. Photonics **4**, 518 (2010).

[12] R. Ding, T. Baehr-Jones, W.-J. Kim, A. Spott, M. Fournier, J.-M. Fedeli, S. Huang, J. Luo, A. K.-Y. Jen, L. Dalton, and M. Hochberg, "Sub-Volt Silicon-Organic Electro-optic Modulator With 500 MHz Bandwidth," J. Lightwave Technol. **29**, 1112 (2011).

[13] Yoshihiro Ogiso, Josuke Ozaki, Yuta Ueda, Norihide Kashio, Nobuhiro Kikuchi, Eiichi Yamada, Hiromasa Tanobe, Shigeru Kanazawa, Hiroshi Yamazaki, Yoshitaka Ohiso, Takuro Fujii, and Masaki Kohtoku, "Over 67 GHz Bandwidth and 1.5 V V_π InP-Based Optical IQ Modulator With n-i-p-n Heterostructure," J. Lightwave Technol. **35**, 1450-1455 (2017)

[14] F. Eltes, J. Fompeyrine, and S. Abel, "$BaTiO_3$-based modulators for integrated optical interconnects," Proc. Of SPIE 10924 (2019).

[15] C. Wang, M. Zhang, B. Stern, M. Lipson, and M. Loncar, "Nanophotonic lithium niobate electro-optic modulators." Opt. Express **26**, 1547 (2018).

[16] M. De Micheli, J. Botineau, P. Sibillot, D. B. Ostrowsky, and M. Papuchon, "Fabrication and characterization of titanium indiffused proton exchanged (TIPE) waveguides in lithium niobate," Opt. Commun. 42(2), 101–103 (1982).

[17] Saleh, Bahaa E. A., and Malvin Carl Teich. *Fundamentals of Photonics*. (Wiley-Interscience, 2007).

[18] M. Levy, R. M. Osgood, Jr., R. Liu, L. E. Cross, G. S. Cargill III, A. Kumar, and H. Bakhru, "Fabrication of single-crystal lithium niobate films by crystal ion slicing," Appl. Phys. Lett. 73(16), 2293–2295 (1998).

[19] Rabiei, Payam, and William H. Steier, "Lithium Niobate Ridge Waveguides and Modulators Fabricated Using Smart Guide," Applied Physics Letters, **86**(16) (2005).

[20] Abu Naim R. Ahmed, Sean Nelan, Shouyuan Shi, Peng Yao, Andrew Mercante, and Dennis W. Prather, "Subvolt electro-optical modulator on thin-film lithium niobate and silicon nitride hybrid platform," Opt. Lett. 45, 1112-1115 (2020)

[21] J. Burghoff, C. Grebing, S. Nolte, and A. Tunnermann, "Efficient frequency doubling in femtosecond laser-written waveguides in lithium niobate," Appl. Phys. Lett. 89, 081108 (2006).

[22] Sung-Mao Wu, Chi-Chang Lai, Hung-Hsiang Cheng, Yu-Che Tai and Chen-Chao Wang, "Frequency dielectric constant and loss tangent extracting of organic material using multi-length microstrip," 2008 International Conference on Electronic Packaging Technology & High Density Packaging, Shanghai (2008).

[23] A. Z. Subramanian et al., "Low-Loss Singlemode PECVD Silicon Nitride Photonic Wire Waveguides for 532–900 nm Wavelength Window Fabricated Within a CMOS Pilot Line," in IEEE Photonics Journal, vol. 5, no. 6, pp. 2202809-2202809, Dec. 2013

[24] A. Rao and S. Fathpour, "Compact lithium niobate electrooptic modulators," IEEE J. Sel. Top. Quantum Electron., **24**(4), 1-14 (2017).

[25] A. Rao and S. Fathpour, "Heterogeneous Thin-Film Lithium Niobate Integrated Photonics for Electrooptics and Nonlinear Optics," IEEE J. Sel. Top. Quantum Electron., **24**(6), 1-12 (2018).

[26] Andrew J. Mercante, Shouyuan Shi, Peng Yao, Linli Xie, Robert M. Weikle, and Dennis W. Prather, "Thin film lithium niobate electro-optic modulator with terahertz operating bandwidth," Opt. Express **26**(11) 14810-14816 (2018).

[27] T. Ren, M. Zhang, C. Wang, L. Shao, C. Reimer, Y. Zhang, O. King, R. Esman, T. Cullen, and M. Loncar, "An Integrated Low-Voltage Broadband Lithium Niobate Phase Modulator," IEEE Photon. Technol. Lett., **31**, 889 (2019).

[28] D. L. K. Eng, B. C. Olbricht, S. Shi, and D. W. Prather, "Dielectric characterization of thin films using microstrip ring resonators," Microw. Opt. Technol. Lett., vol. 57, no. 10, pp. 2306–2310, Oct. 2015.

[29] C. Wang, M. Zhang, X. Chen, M. Bertrand, A. Shams-Ansari, S. Chandrasekhar, P. Winzer, and M. Loncar. "Integrated Lithium Niobate Electro-Optic Modulators Operating at CMOS-Compatible Voltages," Nature 562(7725), 101 (2018).

[30] A. Honardoost, F. A. Juneghani, R. Safian, and S. Fathpour, "Towards subterahertz bandwidth ultracompact lithium niobate electrooptic modulators," Opt. Express **27**, 6495 (2019).

[31] Andrew J. Mercante, David L. K. Eng, Matthew Konkol, Peng Yao, Shouyuan Shi, and Dennis W. Prather, "Thin LiNbO3 on insulator electro-optic modulator," Opt. Lett. **41**(5), 867-869 (2016).

[32] Abu Naim R. Ahmed, Andrew Mercante, Shouyuan Shi, Peng Yao, and Dennis W. Prather, "Vertical mode transition in hybrid lithium niobate and silicon nitride-based photonic integrated circuit structures," Opt. Lett. **43**(17), 4140-4143 (2018).

[33] D. L. K. Eng, S. T. Kozacik, I. V. Kosilkin, J. P. Wilson, D. D. Ross, S. Shi, L. Dalton, B. C. Olbricht, and D. W. Prather, "Simple fabrication and processing of an all-polymer electrooptic modulator," IEEE J. Sel. Top. Quantum Electron. **19**(6), 190–195 (2013).

[34] G. Poberaj, H. Hu, W. Sohler, and P. Günter, "Lithium niobate on insulator (LNOI) for micro-photonic devices," Laser Photonics Rev. 6(4), 488–503 (2012).

[35] I. Krasnokutska, J. J. Tambasco, X. Li, and A. Peruzzo, "Ultra-low loss photonic circuits in lithium niobate on insulator," Opt. Express 26(2), 897–904 (2018).

[36] Han, Huangpu & Xiang, Bingxi. (2019). Simulation and analysis of electro-optic tunable microring resonators in silicon thin film on lithium niobate. Scientific Reports. 9. 10.1038/s41598-019-42818-2.

[37] Lutong Cai, Shuang Li Huangpu Han, and Hui Hu, "Waveguides in single-crystal lithium niobate thin film by proton exchange," Opt. Express 23, 1240-1248 (2015)

APPENDIX

PERMISSIONS

Chapter 6 of this thesis, "LOW-FREQUENCY PHASE MODULATOR IN TFLN AT 1064 NM," re-uses text and figures from the publication, "Thin Film Lithium Niobate Electro-Optic Modulator for 1064 nm Wavelength," published in 2021 in IEEE Photonics Technology Letters.

The IEEE does not require individuals working on a thesis to obtain a formal reuse license, however, the following statement is included as a permission grant:

Requirements to be followed when using any portion (e.g., figure, graph, table, or textual material) of an IEEE copyrighted paper in a thesis:

1) In the case of textual material (e.g., using short quotes or referring to the work within these papers) users must give full credit to the original source (author, paper, publication) followed by the IEEE copyright line © 2021 IEEE.
2) In the case of illustrations or tabular material, we require that the copyright line © 2021 IEEE appear prominently with each reprinted figure and/or table.
3) If a substantial portion of the original paper is to be used, and if you are not the senior author, also obtain the senior author's approval.

Requirements to be followed when using an entire IEEE copyrighted paper in a thesis:

1) The following IEEE copyright/ credit notice should be placed prominently in the references: © 2021 IEEE. Reprinted, with permission, from [author names, paper title, IEEE publication title, and month/year of publication]
2) Only the accepted version of an IEEE copyrighted paper can be used when posting the paper or your thesis on-line.
3) In placing the thesis on the author's university website, please display the following message in a prominent place on the website: In reference to IEEE copyrighted material which is used with permission in this thesis, the IEEE does not endorse any of University of Delaware's products or services. Internal or personal use of this material is permitted. If interested in reprinting/republishing IEEE copyrighted material for advertising or promotional purposes or for creating new collective works for resale or redistribution, please go to http://www.ieee.org/publications_standards/publications/rights/rights_link.html to learn how to obtain a License from RightsLink.

If applicable, University Microfilms and/or ProQuest Library, or the Archives of Canada may supply single copies of the dissertation.